Preparation and Properties of *tetrahedro*-Tetraphosphorus Complexes of Rhodium and Iridium. Molecular and Electronic Structure of $[RhCl(\eta^2\text{-}P_4)(PPh_3)_2]$

Alvin P. Ginsberg,*[1a,b] W. Edward Lindsell,*[1c] Kevin J. McCullough,*[1c] Charles R. Sprinkle,[1a] and Alan J. Welch*[1d]

Contribution from AT&T Bell Laboratories, Murray Hill, New Jersey 07974, Department of Chemistry, Heriot-Watt University, Riccarton, Edinburgh EH14 4AS, U.K., and Department of Chemistry, University of Edinburgh, Edinburgh EH9 3JJ, U.K. *Received August 7, 1985*

Abstract: White phosphorus dissolved in dichloromethane or diethyl ether at −78 °C reacts with the Rh(I) or Ir(I) complexes $[MXL_3]$ (M = Rh, X = Cl, Br, I, L = PPh_3; M = Rh, X = Cl, L = $P(p\text{-tol})_3$, $P(m\text{-tol})_3$, $AsPh_3$; M = Ir, X = Cl, L = PPh_3) to form yellow or orange *tetrahedro*-tetraphosphorus complexes $[MX(P_4)L_2]$. ^{31}P NMR spectroscopy of $[RhX(P_4)(PPh_3)_2]$ in CD_2Cl_2 at low temperatures shows the P_4 ligand to be η^2-coordinated and deshielded by ca. 240 ppm relative to free P_4. The P_4 units act as A_2B_2 spin systems coupling to two ^{31}P nuclei of PPh_3 ligands (X_2) and to ^{103}Rh ($I = 0.5$) to give an overall $A_2B_2MX_2$ spin system. The vibrational frequencies of the P_4 molecule in the rhodium complexes have been identified by infrared and Raman spectroscopy and are found to be from 15 to 90 cm^{-1} lower in energy than the corresponding frequencies in free P_4. An X-ray structure determination on $[RhCl(P_4)(PPh_3)_2]\cdot 2CH_2Cl_2$ at 185 K shows the crystals to be triclinic, space group $P\bar{1}$, with a = 11.853 (2) Å, b = 12.568 (8) Å, c = 14.505 (2) Å, α = 104.41 (4)°, β = 103.42 (13)°, γ = 84.22 (4)°, V = 2033.5 (19) Å^3, D_o = 1.58 g cm^{-3}, Z = 2, and D_c = 1.562 g cm^{-3}. The P_4 molecule is η^2-bonded to the rhodium atom (mean Rh–P = 2.293 Å) with the metal-bonded P–P edge standing perpendicular to the remaining coordination plane of the metal. The phosphine ligands are bent away from the tetraphosphorus group toward the chlorine ($\angle Ph_3P\text{–}Rh\text{–}PPh_3$ = 166.10 (5)°). The bonded edge of the P_4 molecule (P–P = 2.4616 (22) Å) is lengthened by ca. 0.25 Å compared to the edge of a free P_4 molecule; the nonbonded edges are essentially unchanged from the free molecule. EHMO and SCF-Xα-SW calculations on $[RhCl(P_4)(PH_3)_2]$ support the analogy between η^2-bonded P_4 and η^2-bonded alkene or S_2; the "back-bonding" component may be traced to a three-orbital–four-electron interaction between P_4 and the $RhCl(PH_3)_2$ fragment. The Xα calculations show that the most important contribution to the Rh–P_4 covalent bond comes from an equatorial in-plane π overlap of Rh $4d_{yz}$ with a P_4 $2P\pi^*_{\parallel}$ orbital. There is also a contribution from σ overlap of an Rh ($4d_{z^2}$, $4d_{x^2-y^2}$, 5s) hybrid orbital with a P_4 $2P(p_\sigma, \pi_{\parallel}, s_\sigma)$ hybrid. The calculated P–P bond order is 0.4 for the bonded edge and 1.0 for the opposite tetrahedral edge of the P_4 ligand. In an EPA glass at liquid nitrogen temperature $[RhX(P_4)(PPh_3)_2]$ (X = Cl, Br) shows five absorptions in the 700–260-nm region. These are assigned to one-electron transitions, with good agreement between the observed and calculated energies. The absorptions owe most of their intensity to metal → P_4 and metal → phosphine charge transfer.

The bonding of the tetrahedral P_4 allotrope of elemental phosphorus has long interested theoreticians.[2] In marked contrast to N_2, the diatomic species P_2 is only formed at high temperatures, being unstable relative to P_4 by ca. 226 kJ mol^{-1}.[3] Although the bonding in P_4 is principally s and p in character,[4-8] recent calculations[9] show that d-orbital participation is important in making the $2P_2 \rightarrow P_4$ isomerization enthalpy negative. The P_4 molecule may be described either in terms of localized orbitals and "bent" bonds or in terms of delocalized four-center bonding orbitals. Irrespective of the bonding model, the unsaturated nature of P_4 makes it a potential ligand in transition-metal complexes, and the presence of both donor and unoccupied acceptor orbitals should favor its binding to coordinatively unsaturated, low-oxidation-state species such as formed by group VIII (8–10) metals.[6,2] Also, η^1, η^2, and η^3 modes of bonding by P_4 to a metal appear to be feasible.

In recent years Sacconi and co-workers[10] have shown that P_4 is cleaved by a range of transition-metal salts in the presence of polyphosphine ligands to give η^3-P_3 complexes in which the P_3 group may be η^3-coordinated to one or two metals; in the former case the η^3-P_3 ligand may also be η^1-bonded to up to three other metal centers. The rhodium and iridium species $[M(\eta^3\text{-}P_3)(triphos)]$ (M = Rh, Ir; triphos = $(PPh_2CH_2)_3CCH_3$)[11] and the bimetallic cations $[MM'(triphos)_2(\mu\text{-}\eta^3\text{-}P_3)]^{2+}$ (M = Rh, M' = Co, Rh, Ni; M = Ir, M' = Co)[12] are of particular relevance to this paper. Other reported complexes with P_n (n = 1–3) fragments as ligands include cobalt derivatives containing tetrahedral $Co_{4-n}P_n$ units.[13] The structure of $[Co_2(CO)_5(PPh_3)(\mu\text{-}P_2)]$ has been established by X-ray diffraction.[14]

Complexes [M(np)] (M = Ni,[15] Pd;[16] np = $N(CH_2CH_2PPh_2)_3$), which contain a flexible triphosphorus–nitrogen ligand, react with white phosphorus to form insoluble complexes having intact P_4 ligands, [M(P_4)(np)]; X-ray analysis for M = Ni has shown the presence of a η^1-P_4 group.[15] One other complex in which there may be a P_4 ligand is $[Fe_3(CO)_{12}(P_4)]$, but this has not been completely structurally characterized.[17]

Herein we describe syntheses, characterization, and physical, chemical, and theoretical studies of *tetrahedro*-tetraphosphorus complexes of rhodium and iridium having general formula

(1) (a) AT&T Bell Laboratories. (b) After 1985, correspondence for A.P.G. should be addressed to P.O. Box 986, New Providence, NJ 07974. (c) Heriot-Watt University. (d) University of Edinburgh.
(2) Arnold, J. R. *J. Chem. Phys.* **1946**, *14*, 351. Mashima, M. *Ibid.* **1952**, *20*, 801. Pauling, L.; Simonetta, M. *Ibid.* **1952**, *20*, 29.
(3) *Natl. Stand. Ref. Data Ser. (U.S., Natl. Bur. Stand.)* 2nd Ed., **1971**. *NBS Tech. Note (U.S.)* **1968**, No. 270-3.
(4) Archibald, R. M.; Perkins, P. G. *J. Chem. Soc. D* **1970**, 569.
(5) Brundle, C. R.; Kuebler, N. A.; Robin, M. B.; Basch, H. *Inorg. Chem.* **1972**, *11*, 20.
(6) Guest, M. F.; Hillier, I. H.; Saunders, V. R. *J. Chem. Soc., Faraday Trans. 2* **1972**, *68*, 2070.
(7) Osman, R.; Coffey, P.; van Wazer, J. R. *Inorg. Chem.* **1976**, *15*, 287.
(8) Banna, M. S.; Frost, D. C.; McDowell, C. A.; Wallbank, B. *J. Chem. Phys.* **1977**, *66*, 3509.
(9) Trinquier, G.; Malrieu, J.-P.; Daudey, J.-P. *Chem. Phys. Lett.* **1981**, *80*, 552.
(10) Di Vaira, M.; Sacconi, L. *Angew. Chem., Int. Ed. Engl.* **1982**, *21*, 330.
(11) Bianchini, C.; Mealli, C.; Meli, A.; Sacconi, L. *Inorg. Chim. Acta* **1979**, *37*, L543.
(12) Bianchini, C.; Di Vaira, M.; Meli, A.; Sacconi, L. *J. Am. Chem. Soc.* **1981**, *103*, 1448.
(13) Vizi-Orosz, A.; Galamb, V.; Palyi, G.; Marko, L. *J. Organomet. Chem.* **1981**, *216*, 105 and references therein.
(14) Campana, C. F.; Vizi-Orosz, A.; Palyi, G.; Marko, L.; Dahl, L. F. *Inorg. Chem.* **1979**, *18*, 3054.
(15) Dapporto, P.; Midollini, S.; Sacconi, L. *Angew. Chem., Int. Ed. Engl.* **1979**, *18*, 469.
(16) Dapporto, P.; Sacconi, L.; Stoppioni, P.; Zanobini, F. *Inorg. Chem.* **1981**, *20*, 3834.
(17) Schmid, G.; Kempny, H. P. *Z. Anorg. Allg. Chem.* **1977**, *432*, 160.

0002-7863/86/1508-0403$01.50/0

$[MX(P_4)L_2]$ (M = Rh, Ir; L = PR_3, $AsPh_3$; X = halogen), for which η^2-coordination of P_4 has been confirmed when M = Rh, L = PPh_3.[18]

Experimental Section

All procedures were carried out by using Schlenk techniques under an atmosphere of dry, dioxygen-free dinitrogen or under vacuum. Reagent grade solvents were distilled under dinitrogen after refluxing with appropriate drying reagents, as follows: hydrocarbons with CaH_2 or Na metal, ethers with $LiAlH_4$ or $Na[OCPh_2]$, and dichloromethane with P_4O_{10}.

Elemental analyses were determined variously by Analytische Laboratorien, Engelskirchen, West Germany, by Galbraith Laboratories, Knoxville, TN, by Schwarzkopf Laboratory, Woodside, NY, and by Butterworth Laboratories, Teddington, UK. Melting points were measured in evacuated tubes and are uncorrected. Molecular weights were determined at 37 °C by using a vapor pressure osmometer (Mechrolab-Hewlett Packard); readings for decomposing solutions were taken every 5 min and extrapolated back to zero time.

$^{31}P\{^1H\}$ NMR spectra were recorded at 81.02 MHz by using a Bruker WP 200 SY spectrometer at various temperatures and, for $[RhCl(P_4)(PPh_3)_2]$, also at 145.8 MHz by using a Bruker 360 instrument at the University of Edinburgh; CD_2Cl_2 was employed as solvent and 85% H_3PO_4 as external reference. IR spectra were recorded on Perkin-Elmer 457 (4000–300 cm^{-1}) and Beckman IR 11 (500–80 cm^{-1}) instruments; IR frequencies above 500 cm^{-1} were measured on pressed CsI disks and below 500 cm^{-1} on Nujol mulls between polyethylene plates. Raman spectra were determined with a Spex Ramalog instrument on polycrystalline samples in evacuated capillaries using 6471-Å excitation for phosphine complexes and 5682-Å excitation for the triphenylarsine derivative.

Samples for optical spectroscopy were prepared by dissolving $[RhX(P_4)(PPh_3)_2]$ (X = Cl, Br) in CH_2Cl_2 at −35 °C and diluting with EPA (5:5:2 volume ratio of ethyl ether–isopentane–ethyl alcohol) that had been cooled to the same temperature. Concentrations ranged from 1×10^{-3} to 1×10^{-6} M, and the final mixture contained 5–10% CH_2Cl_2. The cold solutions were transferred via a stainless steel tube to a stainless steel cell (path length, 1.915 cm) fitted with Suprasil windows and containing a liquid-nitrogen filled stainless steel insert provided with an opening through which the spectrophotometer beam could pass. An evacuated ($\sim 1 \times 10^{-6}$ mmHg) stainless steel container, also fitted with Suprasil windows, enclosed the cell. The samples froze to clear transparent glasses. Spectra of the glasses were measured in the 250–800-nm region with a Cary Model 14R spectrophotometer. Extinction coefficients were corrected for solvent contraction by multiplying by 0.771, the fractional change in volume of EPA on cooling from +20 to −196 °C.[19]

Starting Materials. White phosphorus was freshly cut from the center of a stick (Alfa), washed well with water, and dried under vacuum at 10^{-3} mmHg for ca. 20 min before use. The following complexes were prepared by literature methods: $[RhX(PPh_3)_3]$ (X = Cl, Br, I),[20] $[RhCl(AsPh_3)_3]$,[21] $[RhCl(cyclooctene)_2]_2$,[22] and $[IrCl(PPh_3)_3]$.[23] The complexes $[RhCl(PR_3)_3]$ (R = *p*-tol, *m*-tol) were synthesized by reaction of the appropriate phosphine with $[RhCl(cyclooctene)_2]_2$; other phosphine derivatives of Rh(I) were formed by similar reactions (cf. ref 24).

$[RhCl(P_4)(PPh_3)_2]$. A solution of white phosphorus (70 mg, 0.56 mmol) in dichloromethane (20 mL) was added dropwise, over 15 min, to a stirred solution of $[RhCl(PPh_3)_3]$ (500 mg, 0.54 mmol) in dichloromethane (15 mL) at −78 °C. After stirring for a further 45 min at −78 °C, the color of the solution had changed from deep red to yellow. Dropwise addition of diethyl ether (200 mL) to the still cold solution precipitated the product as a yellow microcrystalline solid which was washed with ether and dried at 82 °C (10^{-3} mmHg); yield 305 mg (72%). Anal. Found: C, 54.8; H, 4.0; P, 23.5; Cl, 4.7. Calcd: C, 54.95; H, 3.8; P, 23.6; Cl, 4.5.

$[RhBr(P_4)(PPh_3)_2]$. In a similar procedure to the above reaction, white phosphorus (76 mg, 0.61 mmol) in CH_2Cl_2 (35 mL) and $[RhBr(PPh_3)_3]$ (600 mg, 0.62 mmol) in CH_2Cl_2 (15 mL) were reacted at −78 °C. The yellow solid, 375 mg (73%), was washed with ether and dried at 82 °C (10^{-3} mmHg). Anal. Found: C, 51.9; H, 4.05; P, 22.3; Br, 9.8. Calcd: C, 52.0; H, 3.6; P, 22.4; Br, 9.6.

$[RhI(P_4)(PPh_3)_2]$. As above, P_4 (75 mg, 0.60 mmol) and $[RhI(PPh_3)_3]$ (600 mg, 0.59 mmol) gave the product (440 mg, 85%). Anal. Found: C, 49.1; H, 3.3; P, 21.1; I, 14.4. Calcd: C, 49.2; H, 3.4; P, 21.2; I, 14.45.

$[RhCl(P_4)(P(p\text{-tol})_3)_2]$. A solution of white phosphorus (65 mg, 0.52 mmol) in CH_2Cl_2 (15 mL) was added dropwise to a stirred solution of $[RhCl(P(p\text{-tol})_3)_3]$ (500 mg, 0.48 mmol) in diethyl ether (30 mL) at −78 °C. The mixture was then stirred for 2 h at −78 °C before hexane (150 mL) was added to precipitate the yellow product. This solid was collected by filtration at low temperature; reduction in the volume of the cold filtrate afforded further solid product. The combined products were washed with hexane and dried in vacuo at room temperature; total yield 260 mg (63%). Anal. Found: C, 58.2; H, 5.0; P, 21.1; C, 3.9. Calcd: C, 57.9; H, 4.9; P, 21.3; Cl, 4.1.

$[RhCl(P_4)(P(m\text{-tol})_3)_2]$. A solution of white phosphorus (65 mg, 0.52 mmol) in diethyl ether (25 mL) was added dropwise over 30 min to a solution of $[RhCl(P(m\text{-tol})_3)_3]$ (500 mg, 0.48 mmol) in ether (100 mL) at −78 °C. The mixture was stirred at −78 °C for a further 1.25 h before hexane (125 mL) was added slowly at −78 °C. Filtration of the resulting cold mixture gave a small quantity of solid product (ca. 30 mg). Reduction in volume of the cold filtrate (to ca. 60 mL) produced more product which was collected, washed with hexane, and dried in vacuo at room temperature; combined yield 230 mg (55%). Anal. Found: C, 57.4; H, 4.8; P, 21.6; Cl, 4.0. Calcd: C, 57.9; H, 4.9; P, 21.3; Cl, 4.1.

$[RhCl(P_4)(AsPh_3)_2]$. White phosphorus (80 mg, 0.65 mmol) in CH_2Cl_2 (25 mL) was added dropwise to a solution of $[RhCl(AsPh_3)_3]$ (600 mg, 0.59 mmol) in CH_2Cl_2 (20 mL) at −78 °C over 30 min. After stirring for a further 1 h, ether (200 mL) was added to the cold solution to precipitate the yellow product which was washed well with ether and dried at room temperature in vacuo (10^{-3} mmHg): yield 210 mg (42%). Anal. Found: C, 49.1; H, 3.3; P, 14.5; As, 17.6; Cl, 4.4. Calcd: C, 49.4; H, 3.5; P, 14.2; As, 17.1; Cl, 4.05.

$[IrCl(P_4)(PPh_3)_2]$. As in the preparation of the Rh analogue, P_4 (75 mg, 0.60 mmol) and $[IrCl(PPh_3)_3]$ (600 mg, 0.59 mmol) in CH_2Cl_2 (35 mL) at −78 °C, after stirring for 4 h, gave the solid orange product in ca. 60% yield on precipitation by ether (150 mL). The solid was washed with ether and dried at 82 °C (10^{-3} mmHg). Anal. Found: C, 49.5; H, 3.45; P, 21.0; Cl, 3.95. Calcd: C, 49.35; H, 3.45; P, 21.2; Cl, 4.05.

Reaction of $[RhCl(P_4)(PPh_3)_2]$ with CO. $[RhCl(P_4)(PPh_3)_2]$ (150 mg, 0.19 mmol) was suspended in CH_2Cl_2 (15 mL) at −78 °C, and CO was passed through the suspension for 2 h. During this time the solid dissolved and then a pale yellow crystalline material precipitated (ca. 70 mg) which was collected by filtration, washed with ether, and dried in vacuo. This product was identified as $[RhCl(CO)(PPh_3)_2]$ by IR spectroscopy and by analysis. Anal. Found: C, 64.0; H, 4.5; P, 9.3; Cl, 5.5. Calcd: C, 64.3; H, 4.4; P, 9.0; Cl, 5.1.

Reaction of $[RhCl(P_4)(AsPh_3)_2]$ with CO. CO was passed through a solution of $[RhCl(P_4)(AsPh_3)_2]$ (250 mg, 0.29 mmol) in CH_2Cl_2 (15 mL) at −78 °C for 2 h. The deep red reaction mixture was filtered while cold. Addition of ether (150 mL) to the filtrate at −78 °C gave a brown precipitate in low yield. This solid was collected by filtration, washed with ether, and dried in vacuo. Anal. Found: C, 34.1; H, 3.4; P, 17.4; As, 10.5. Calcd for $[RhCl(CO)(P_4)(AsPh_3)].1.5CH_2Cl_2$: C, 34.0; H, 2.5; P, 17.1; As, 10.35.

Reaction of $[RhCl(P_4)(PPh_3)_2]$ with dppe. $[RhCl(P_4)(PPh_3)_2]$ (70 mg, 0.09 mmol) was suspended in CH_2Cl_2 (15 mL) at −78 °C and excess dppe (300 mg) was added. This mixture was stirred for 4 h and then ether (80 mL) was added to precipitate a bright yellow solid which was collected, washed with ether, and dried in vacuo. This product was slightly impure $Rh(dppe)_2Cl$; recrystallization from dichloromethane/benzene gave pure material, although some CH_2Cl_2 of crystallization was retained even after drying at 82 °C (10^{-3} mmHg). Anal. Found: C, 65.2; H, 5.7; P, 12.85; Cl, 4.45. Calcd for $[Rh(dppe)_2]Cl.0.25\ CH_2Cl_2$: C, 65.6; H, 5.1; P, 12.95; Cl, 4.6.

Other Reactions of $[RhX(P_4)(PPh_3)_2]$ (X = Cl, Br, or I). $[RhCl(P_4)(PPh_3)_2]$ (ca. 100 mg) in CH_2Cl_2 was reacted at low temperatures with the following reagents for the durations indicated. The products were isolated by precipitation with ether and/or hexane followed by suitable purification procedures: (i) $[RhCl(PPh_3)_3]$ in CH_2Cl_2 at −63 °C for 1 h; (ii) PEt_3 at −78 °C for 12 h; (iii) PF_3 at −78 °C for 1 h; and (iv) HCl at −78 °C for 0.25 and 1.5 h.

Similarly, $[RhBr(P_4)(PPh_3)_2]$ (ca. 100–150 mg) was reacted with the following: (v) HBr gas for 0.25 h, initially at −78 °C but with some elevation of temperature during the reaction; (vi) H_2 gas at −78 °C for 2 h; and (vii) C_2H_4 gas at −78 °C for 1.5 h. From reactions vi and vii unreacted $[RhBr(P_4)(PPh_3)_2]$ was recovered in essentially quantitative yields.

(18) Preliminary reports of some of this work have been published: (a) Ginsberg, A. P.; Lindsell, W. E. *J. Am. Chem. Soc.* **1971**, *93*, 2082. (b) Lindsell, W. E. *J. Chem. Soc., Chem. Commun.* **1982**, 1422. (c) Lindsell, W. E.; McCullough, K. J.; Welch, A. J. *J. Am. Chem. Soc.* **1983**, *105*, 4487.

(19) Passerini, R.; Ross, I. G. *J. Sci. Instrum.* **1953**, *30*, 274.

(20) Osborn, J. A.; Wilkinson, G. *Inorg. Synth.* **1967**, *10*, 67. Osborn, J. A.; Jardine, F. H.; Young, F. H.; Wilkinson, G. *J. Chem. Soc. A* **1966**, 1711.

(21) Mague, J. T.; Wilkinson, G. *J. Chem. Soc. A* **1966**, 1736.

(22) van der Ent, A.; Onderdelinden, A. L. *Inorg. Synth.* **1973**, *14*, 92.

(23) Bennett, M. A.; Milner, D. L. *J. Am. Chem. Soc.* **1969**, *91*, 6983.

(24) Montelatici, S.; van der Ent, A.; Osborn, J. A.; Wilkinson, G. *J. Chem. Soc. A* **1968**, 1054.

$[RhI(P_4)(PPh_3)_2]$ (150 mg) was reacted with MeI (15 mL) at temperatures between −60 °C and ambient temperature over 0.75 h. Addition of ether to the brown solution gave a brown precipitate which was collected and reprecipitated from CH_2Cl_2 by ether before drying in vacuo (130 mg). No reaction occured between $[RhI(P_4)(PPh_3)_2]$ and MeI at −60 °C.

Structural Characterization of $[RhCl(P_4)(PPh_3)_2]$

Suitable single crystals of $[RhCl(P_4)(PPh_3)_2]$ as a 1:2 solvate were grown at −78 °C from a saturated CH_2Cl_2 solution. To avoid loss of solvent of crystallization a single crystal was rapidly secured inside a Lindemann capillary and mounted directly on an Enraf-Nonius CAD4 diffractometer equipped with a low-temperature attachment (N_2 stream) operating at −85 ± 1 °C.

The cell constants were derived from a least-squares fit of the setting angles of 25 carefully centered reflections in the 2θ range 20–22° (graphite-monochromated Mo Kα X-radiation, $\bar{\lambda}$ = 0.71069 Å).

Crystal Data. $C_{36}H_{30}ClRhP_6 \cdot 2CH_2Cl_2$, M_r = 786.84, triclinic, space group $P\bar{1}$ (C_i^1, No. 2),[25] a = 11.8530 (17) Å, b = 12.568 (8) Å, c = 14.505 (3) Å, α = 104.41 (3)°, β = 103.424 (13)°, γ = 84.22 (4)°, V = 2033.5 (19) Å^3, Z = 2, D_c = 1.562 g cm^{-3}, D_o = 1.58 g cm^{-3}, $F(0,0,0)$ = 986 electrons, μ(Mo K$\bar{\alpha}$) = 9.8 cm^{-1}, crystal dimensions 0.2 ({001}–{00$\bar{1}$}), 0.3 ({100}–{$\bar{1}$00}), and 0.4 ({010}–{0$\bar{1}$0}) mm.

Data Collection. One hemisphere of intensity data ($\pm h, -k, \pm l$) was measured in the 2θ range 2–50° by ω–2θ scans in 96 steps with the ω scan width set by 0.8 + 0.35 tan θ. After a rapid prescan only those reflections considered significantly intense {$I \geq 1.0\sigma(I)$} were remeasured such that the final net intensity had $I \geq 33.0\sigma(I)$, subject to a maximum measuring time of 60 s. Two intensity and two orientation control reflections were remonitored once every 1 h and 300 reflections, respectively, but subsequent analysis of the net intensities of the former showed no significant change over the ca. 124 h of X-ray exposure. Of 7137 unique data measured, 5245 had $F \geq 2.0\sigma(F)$ and were retained. No correction for X-ray absorption was applied.

Structure Solution and Refinement. The rhodium atom was readily located from a Patterson map, and all other non-hydrogen atoms were found by an iterative combination of full-matrix least-squares refinement and ΔF syntheses. Ultimately all non-H atoms except the methylene carbon atoms were allowed anisotropic thermal motion. Phenyl groups were treated as rigid, planar hexagons (C–C = 1.395 Å), and all hydrogen atoms were set in idealized positions (C–H = 1.08 Å) with fixed thermal parameters (U[26] = 0.08 Å^2 for methylene H's; otherwise 0.05 Å^2). The weighting scheme $w^{-1} = \sigma^2(F) + 0.003376(F^2)$ gave satisfactory analysis of variance as a function of $(\sin\theta)/\lambda$, F, h, k, and l. At convergence the R factors[27] were R = 0.0456 and R_w = 0.0625. The final ΔF map was featureless except for two residues ca. 0.9 e Å^{-3} in the vicinity of the solvent molecules. Table I lists derived fractional coordinates. Thermal parameters (Table II), hydrogen atom coordinates, and a comparison of calculated and observed structure factor amplitudes (×10) are available as supplementary material.

All crystallographic calculations were carried out by using SHELX76[28] and XANADU,[29] and plots were constructed by using ORTEP-II[30] and SCHAKAL.[31]

Procedures for Molecular Orbital Calculations

EHMO calculations were performed using a locally adapted version of ICON8[32] implemented on an ICL 2972 computer. The molecule *trans*-$[RhCl(P_4)(PH_3)_2]$ and the fragment *trans*-$[RhCl(PH_3)_2]$ were studied in strict C_{2v} symmetry and square-planar metal geometry, with a 180° torsion angle in the atomic sequence Cl–Rh–P–H (in plane). The P_4 function was strictly tetrahedral. Pertinent parameters are Rh–PH_3 2.33 Å, Rh–P_4 2.25 Å, Rh–Cl 2.41 Å, P–H 1.42 Å, and P–P 2.21 Å; Rh–P–H

Table I. Fractional Coordinates of Atoms with Standard Deviations

	x	y	z
Rh(1)	0.21154 (3)	0.40539 (3)	0.35212 (3)
Cl(1)	0.15653 (11)	0.31181 (11)	0.18293 (9)
P(1)	0.22466 (11)	0.22676 (11)	0.37486 (9)
P(2)	0.19058 (11)	0.56188 (11)	0.28966 (10)
P(3)	0.16976 (13)	0.49092 (12)	0.50099 (10)
P(4)	0.36859 (12)	0.46662 (12)	0.47262 (11)
P(5)	0.30510 (15)	0.61297 (13)	0.56967 (11)
P(6)	0.32533 (16)	0.45419 (14)	0.60958 (11)
C(2)	0.19287 (23)	0.2285 (3)	0.55834 (23)
C(3)	0.22505 (23)	0.2142 (3)	0.65343 (23)
C(4)	0.33495 (23)	0.1690 (3)	0.68655 (23)
C(5)	0.41266 (23)	0.1382 (3)	0.62457 (23)
C(6)	0.38048 (23)	0.1525 (3)	0.52948 (23)
C(1)	0.27058 (23)	0.1977 (3)	0.49636 (23)
C(8)	0.4408 (3)	0.18543 (23)	0.32862 (23)
C(9)	0.5225 (3)	0.13120 (25)	0.27567 (23)
C(10)	0.4924 (3)	0.03870 (25)	0.20019 (23)
C(11)	0.3805 (3)	0.00043 (25)	0.17767 (23)
C(12)	0.2987 (3)	0.05467 (25)	0.23062 (23)
C(7)	0.3289 (3)	0.14717 (25)	0.30610 (23)
C(14)	−0.0154 (3)	0.22236 (22)	0.3069 (3)
C(15)	−0.1224 (3)	0.17338 (22)	0.2772 (3)
C(16)	−0.1280 (3)	0.06168 (22)	0.2722 (3)
C(17)	−0.0265 (3)	−0.00103 (22)	0.2969 (3)
C(18)	0.0806 (3)	0.04795 (22)	0.3267 (3)
C(13)	0.0861 (3)	0.15965 (22)	0.3317 (3)
C(20)	0.10005 (22)	0.7444 (3)	0.4062 (3)
C(21)	0.10394 (22)	0.8459 (3)	0.4731 (3)
C(22)	0.20687 (22)	0.9018 (3)	0.5058 (3)
C(23)	0.30592 (22)	0.8562 (3)	0.4716 (3)
C(24)	0.30204 (22)	0.7547 (3)	0.4047 (3)
C(19)	0.19910 (22)	0.6988 (3)	0.3720 (3)
C(26)	0.3082 (3)	0.6562 (3)	0.1844 (3)
C(27)	0.3971 (3)	0.6600 (3)	0.1371 (3)
C(28)	0.4783 (3)	0.5719 (3)	0.1255 (3)
C(29)	0.4705 (3)	0.4802 (3)	0.1611 (3)
C(30)	0.3815 (3)	0.4765 (3)	0.2084 (3)
C(25)	0.3004 (3)	0.5645 (3)	0.2200 (3)
C(32)	−0.0459 (3)	0.5305 (3)	0.23741 (22)
C(33)	−0.1574 (3)	0.5302 (3)	0.17874 (22)
C(34)	−0.1769 (3)	0.5663 (3)	0.09263 (22)
C(35)	−0.0850 (3)	0.6027 (3)	0.06519 (22)
C(36)	0.0264 (3)	0.6030 (3)	0.12387 (22)
C(31)	0.0459 (3)	0.5669 (3)	0.20998 (22)
Cl(2)	0.05876 (25)	0.88372 (24)	0.07367 (17)
Cl(3)	0.2082 (4)	0.7623 (3)	−0.04835 (20)
C(37)	0.0836 (8)	0.8446 (8)	−0.0445 (7)
Cl(4)	0.48912 (23)	0.19445 (19)	1.01865 (19)
Cl(5)	0.25881 (24)	0.1125 (3)	0.94643 (20)
C(38)	0.3462 (6)	0.2044 (6)	1.0369 (5)

Table III. Parameters Used in EHMO Calculations[a]

orbital	H_{ii}, eV	ζ_1	orbital	H_{ii}, eV	ζ_1
H 1s	−13.60	1.30	Cl 3p	−15.00	2.033
P 3s	−18.60	1.60	Cl 3d	−9.00	2.033
P 3p	−14.00	1.60	Rh 5s	−8.09	2.135
P 3d	−7.00	1.40	Rh 5p	−4.57	2.10
Cl 3s	−30.00	2.033	Rh 4d	−12.50	4.29[b]

[a] H_{ii}'s and orbital exponents for H, Cl, and P (with d orbitals included for the last two) are those inlaid in the ICON8 program. For Rh, values used were taken from: Hoffman, D. M.; Hoffmann, R.; Fisel, C. R. *J. Am. Chem. Soc.* **1982**, *104*, 3858–3875. (Lower set of values of their Table III.) [b] c_1 = 0.5807, ζ_2 = 1.97, c_2 = 0.5685.

(25) "International Tables for X-Ray Crystallography"; Kynoch Press: Birmingham, England, 1974; Vol. IV.
(26) The isotropic thermal parameter is defined as $\exp[8\pi^2 U(\sin^2\theta)/\lambda^2]$.
(27) $R = \sum||F_o| - |F_c||/\sum|F_o|$; $R_w = \sum w^{1/2}||F_o| - |F_c||/\sum w^{1/2}|F_o|$.
(28) Sheldrick, G. M., University Chemical Laboratory, Cambridge, England, 1976.
(29) Roberts, P.; Sheldrick, G. M., University Chemical Laboratory, Cambridge, England, 1976.
(30) Johnson, C. K. Report ORNL-5183, Oak Ridge National Laboratory, Tennessee, 1976.
(31) Keller, E. University of Freiburg, F.R.G., 1980.
(32) Howell, J.; Rossi, A.; Wallace, D.; Haraki, K.; Hoffmann, R. *QCPE* **1977**, *10*, 344.

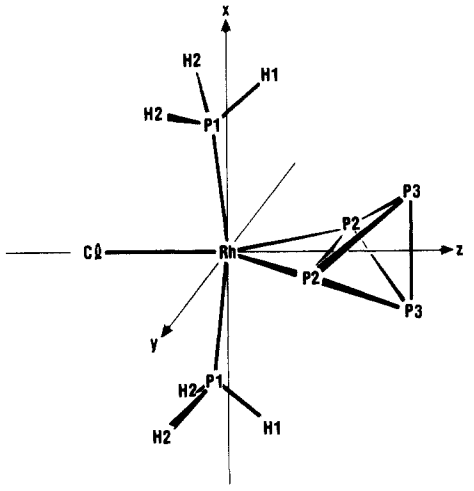

Figure 1. Coordinate axes, conformation, and atom numbering scheme for molecular orbital calculations.

and H–P–H 109.47°. The values of the H_{ii}'s and orbital exponents used are given in Table III.

SCF–Xα–SW calculations[33,34] were carried out on a Cray-1 computer with a current version of the Xα–SW program package.[35] Figure 1 shows the coordinate axes, conformation, and atom numbering for the C_{2v} model complex $[RhCl(\eta^2\text{-}P_4)(PH_3)_2]$. P1 labels the phosphine phosphorus atoms, P2 the phosphorus atoms of the bound P_4 edge, and P3 the phosphorus atoms of the opposite tetrahedral edge. Coordinates in atomic units (1 bohr = 0.529 17 Å) were derived from the bond distances and angles found in the structure of $[RhCl(\eta^2\text{-}P_4)(PPh_3)_2]$ and from d(P–H) and ∠H–P–H in the PH_3 molecule.[36] Overlapping atomic-sphere radii were taken as 89% of the atomic number radii;[37] the values are as follows (in bohrs): Rh, 2.470 19; Cl, 2.698 88; P1, 2.363 43; P2, 2.432 92; P3, 2.469 32; H1, 1.475 76; and H2, 1.478 38. These values gave a satisfactory virial ratio ($-2T/V$ = 1.000 261). The outer sphere surrounding the molecule was centered at the valence electron weighted average of the atom positions and was taken tangent to the P3 spheres, giving an outer-sphere radius of 9.1739 bohrs. α exchange–correlation parameter values were as follows:[38,39] α_{Rh} = 0.702 17, α_{Cl} = 0.723 25, α_P = 0.726 20, and α_H = 0.777 25. In the extramolecular and intersphere regions α was taken as an average of the atomic-sphere α values weighted by the number of valence electrons in the neutral atoms: $\alpha_{OUT} = \alpha_{INT}$ = 0.728 20.

The initial cluster potential for $[RhCl(P_4)(PH_3)_2]$ was constructed by superposing SCF–Xα charge densities for Rh^0, Cl^0, P^0 and H^0. Partial waves through l = 5 in the extramolecular region, l = 3 in the rhodium sphere, l = 2 in the phosphorus and chlorine spheres, and l = 0 in the hydrogen spheres were used to expand the wave functions. C_{2v} symmetry was used to factor the secular matrix. The spin-restricted ground-state calculations required about 11 s of Cray-1 processor time per iteration and converged in 47 iterations to ±0.0001 Ry or better for the valence levels. A weighted average of the initial and final potential for a given iteration was used as the starting potential for the next iteration; the proportion of final potential in the average was 10–15%.

(33) Slater, J. C. "The Self-Consistent Field for Molecules and Solids: Quantum Theory of Molecules and Solids"; McGraw-Hill: New York, 1974; Vol. 4.
(34) Slater, J. C. "The Calculation of Molecular Orbitals"; Wiley: New York, 1979.
(35) Locally modified version of the revision by Mike Cook, Bruce Bursten, and George Stanly.
(36) Kuchitsu, K. J. *Mol. Spectrosc.* **1961**, *7*, 399. Sirvetz, M. H.; Weston, R. E. *J. Chem. Phys.* **1953**, *21*, 898.
(37) Norman, J. G., Jr. *Mol. Phys.* **1976**, *31*, 1191.
(38) Schwarz, K. *Phys. Rev. B: Solid State* **1972**, *5*, 2466. Schwarz, K. *Theor. Chim. Acta* **1974**, *34*, 225.
(39) Slater, J. C. *Int. J. Quantum Chem., Symp.* **1973**, *7*, 533.
(40) Intille, G. M. *Inorg. Chem.* **1972**, *11*, 695.

Table IV. Physical Properties of P_4 Complexes

complex	color	mp, °C	mol wt found	mol wt calcd
$[RhCl(P_4)(PPh_3)_2]$ (**1**)	yellow	171–173 d	*a*	
$[RhBr(P_4)(PPh_3)_2]$ (**2**)	yellow	d 166–168		
$[RhI(P_4)(PPh_3)_2]$ (**3**)	yellow	d 153–156		
$[RhCl(P_4)(P(p\text{-tol})_3)_2]$ (**4**)	yellow	132–134 d	760,[b] 920[c]	871
$[RhCl(P_4)(P(m\text{-tol})_3)_2]$ (**5**)	yellow	d 110–115	765[c]	871
$[RhCl(P_4)(AsPh_3)_2]$ (**6**)	yellow	d 104–106	700,[b] *a*	875
$[IrCl(P_4)(PPh_3)_2]$ (**7**)	orange	d 158–161		

[a] P_4^+ peak in mass spectrum. [b] In $CHCl_3$. [c] In benzene.

The final $[RhCl(P_4)(PH_3)_2]$ ground-state potential was used to search for virtual levels up to a maximum energy of –0.05 Ry; it also served as the starting point for SCF calculations of the Slater transition states for one-electron transitions to the virtual levels.[33,34] The transition-state calculations were carried out in spin-unrestricted form to give estimates for both singlet and triplet transition energies.

Results and Discussion

Syntheses and Reactivity. White phosphorus dissolved in dichloromethane or diethyl ether reacts with solutions of Rh(I) or Ir(I) complexes $[MXL_3]$ (M = Rh, Ir; L = phosphine, arsine; X = halogen). At ambient temperature dark colored products of variable composition are obtained from solution, probably resulting from the presence of differing P_n groups and differing degrees of complex aggregation, accompanied by some oxidation of the coordinated phosphorus. However, at low temperatures, conveniently –78 °C, reaction 1 occurs smoothly to give products

$$[MXL_3] + P_4 \xrightarrow[-78\ °C]{CH_2Cl_2 \text{ or } Et_2O} [MX(P_4)L_2] \qquad (1)$$

1–7 of Table IV in yields of up to 85%. Although reactions do occur between complexes $[MXL_3]$ (M = Rh; X = Cl; L = $P(OPh)_3$, $PEtPh_2$ or PMe_2Ph) and P_4 under similar conditions to those of eq 1, the products are not isolated in analytically pure form, the complete removal of residual solvent being one problem.

Products **1–7** are yellow or orange solids which are moderately air sensitive at ambient temperature but stable under dinitrogen or vacuum. They are soluble in dichloromethane, in chloroform, and, especially complexes **4** and **5**, in aromatic solvents, but these solutions are unstable above ca. –20 °C. Amber prismatic crystals of **1**, suitable for X-ray analysis, can be obtained from solutions in CH_2Cl_2 at –78 °C, but these crystals lose solvent at ambient temperature. At –78 °C dioxygen does not react with solutions of the complexes. At room temperature extensive decomposition occurs in solution within 0.5–1 h under either dinitrogen or dioxygen atmospheres and, as shown by ^{31}P NMR spectroscopy (vide infra), involves dissociation of PPh_3 and some P_4 from complexes **1–3**.

The dark brown solids, obtained after precipitation with ether from solutions of **1** in CH_2Cl_2 that had remained at ambient temperature for over 16 h, varied in composition; IR spectra of these products normally exhibited broad absorption bands around 1000 cm^{-1} and often ν(OH) bands. Thus, one sample had analytical data (C, 37.5; H, 2.9; Cl, 6.0; P, 27.3) consistent with species $[RhCl(P_4O_3)(PPh_3)]_n$ (calcd: C, 37.8; H, 2.6; Cl, 6.2; P, 27.0) containing a P_4O_3 group (or possibly $P_4O_3H_2$). Another sample contained 31.7% C, 3.0% H, consistent with further oxidation to a species such as $[RhCl(P_4O_{10}H_n)(PPh_3)]$ (calcd (n = 0): C, 31.6; H, 2.2; (n = 6): C, 31.3; H, 3.1). These products appear to be easily oxidized, and it is difficult to avoid incorporation of oxygen (and water) on isolation.

Molecular weights of complexes **4–6** were obtained from decomposing solutions by taking readings over a 20-min period and extrapolating back to zero time (see Table IV); these values support monomeric formulas. Mass spectra (electron impact) did not afford parent ions, but both **1** (at 150 °C) and **6** (at 80 °C) gave strong P_4^+ ion peaks.

Complex **2** showed no reaction with dihydrogen or ethylene at –78 °C. Carbon monoxide reacts with complexes **1** and **6** in

Table V. ^{31}P NMR Parameters of η^2-P_4 Complexes $[RhY(P^A_2P^B_2)(P^XPh_3)_2]$ in CD_2Cl_2[a,b]

complex	temp, °C	$\delta(P^A)$	$\delta(P^B)$	$\delta(P^X)$	$^1J(P^A-P^B)$	$^2J(P^X-P^A)$	$^3J(P^X-P^B)$	$^1J(Rh-P^A)$	$^2J(Rh-P^B)$	$^1J(Rh-P^X)$
1, Y = Cl	−22	−279.4	−284.0	43.2	175	4.7	8.6	33.9	0	115.3
2, Y = Br	−21	−276.4	−280.6	41.4	179	4.4	8.6	33.3	0	115.7
3, Y = I	−40	−273.8	−276.8	38.2	182	3.9	10.1	31.4	0	114.6

[a] Chemical shift in ppm to high frequency of 85% H_3PO_4. [b] Coupling constant in Hz (estimated error: <0.5 Hz; $J(P^A-P^B)$ ca. ±2 Hz).

CH_2Cl_2 at −78 °C within 2 h. With **1**, the main product is $[RhCl(CO)(PPh_3)_2]$, formed by P_4 ligand displacement, eq 2.

$$[RhCl(P_4)(PPh_3)_2] + CO \rightarrow [RhCl(CO)(PPh_3)_2] + P_4 \quad (2)$$

With **6**, an $AsPh_3$ ligand is displaced, eq 3; the product was

$$[RhCl(P_4)(AsPh_3)_2] + CO \rightarrow [RhCl(CO)(P_4)(AsPh_3)] + AsPh_3 \quad (3)$$

obtained in solvated form. These two different reaction pathways may be taken to illustrate the relative stabilities of PPh_3, P_4, and $AsPh_3$ ligands bound to Rh(I), although we note that NMR evidence (vide infra) indicates that P_4 is bound differently in the arsine than in the phosphine complex.

Both the P_4 and PPh_3 ligands of complex **1** are substituted by 1,2-bis(diphenylphosphino)ethane (dppe) and by triethylphosphine at −78 °C in CH_2Cl_2. Reaction of **1** with dppe follows eq 4;

$$[RhCl(P_4)(PPh_3)_2] + 2dppe \rightarrow [Rh(dppe)_2]Cl + P_4 + 2PPh_3 \quad (4)$$

reaction with PEt_3 essentially follows eq 5 with the product being

$$[RhCl(P_4)(PPh_3)_2] + 3PEt_3 \rightarrow [RhCl(PEt_3)_3] + P_4 + 2PPh_3 \quad (5)$$

$[RhCl(PEt_3)_3]$ (Anal. Found: C, 44.1; H, 8.9; Cl, 7.4. Calcd: C, 43.9; H, 9.2; Cl, 7.2),[24] although this may be isolated in admixture with $[Rh_2Cl_2(PEt_3)_4]$. Trifluorophosphine also reacts with **1** at −78 °C to give a pale yellow solid for which analytical characterization was inconclusive, but significant loss of coordinated P_4 occurs and the product may be largely $[Rh(PPh_3)_2(PF_3)_2Cl]$.

Hydrogen chloride solubilizes **1** at −78 °C; after 0.25 h only unreacted **1** could be isolated on precipitation, but after 1.5 h distinct reaction occurs, and the incompletely characterized product contains additional chlorine, probably resulting from oxidative addition. Similar observations were noted for interaction of HBr with **2**. Iodomethane does not react with **3** at −60 °C, but on slow warming of the reaction mixture to ambient temperature a dark brown product containing additional iodine (I 30.0%) is obtained, again probably via oxidative addition.

Mixing $[RhCl(PPh_3)_3]$ with an equimolar amount of **1** at −63 °C in CH_2Cl_2 affords $[Rh_2Cl_2(PPh_3)_4]$ (Anal. Found: C, 65.2; H, 4.7; P, 10.6. Calcd: C, 65.2; H, 4.5; P, 9.3) as the main product after crystallization, eq 6.

$$[RhCl(P_4)(PPh_3)_2] + [RhCl(PPh_3)_3] \rightarrow [Rh_2Cl_2(PPh_3)_4] + P_4 + PPh_3 \quad (6)$$

^{31}P NMR Spectra. Complexes **1–3** display well-resolved $^{31}P\{^1H\}$ NMR spectra at low temperatures in CD_2Cl_2 solutions. Resonances assignable to P_4 groups occur at high fields and resonances of magnetically equivalent PPh_3 groups at ca. δ = 40 ppm. The spectra (Figures 2–4) have been analyzed by computer simulation (program PANIC) giving the parameters listed in Table V. The P_4 units act as A_2B_2 spin systems coupling to two ^{31}P nuclei of PPh_3 ligands (X_2) and to ^{103}Rh (I = 0.5) giving an overall $A_2B_2MX_2$ spin system (more correctly an $A_2BB'MXX'$ system with strong coupling between B/B' and between X/X' nuclei). There are chemical shifts of ca. 4 ppm between P^A and P^B nuclei and $^1J(P^A-P^B)$ values lie in the range 175–182 Hz. Spectra of complex **1** have been recorded at both 81.02 and 145.8 MHz at −60 °C, and, although resolution was poorer at the higher fre-

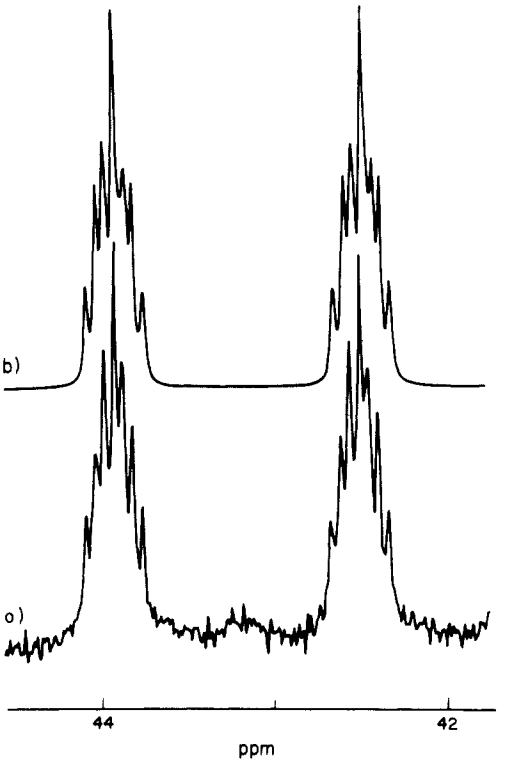

Figure 2. 81.02-MHz $^{31}P\{^1H\}$ NMR spectra of PPh_3 groups of complex **1** in CD_2Cl_2 at −22 °C. (a) Experimental spectrum (line narrowed). (b) Simulated spectrum (PANIC): δ = 43.2 ppm; $^1J(Rh-P)$ = 115.3 Hz; $^2J(P-P^A)$ = 4.7 Hz; $^3J(P-P^B)$ = 8.6 Hz; line width = 2 Hz.

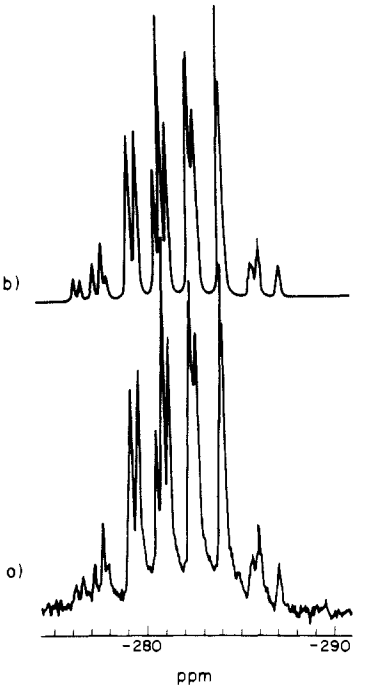

Figure 3. 81.02-MHz $^{31}P\{^1H\}$ NMR spectra of P_4 ligand of complex **1** in CD_2Cl_2 at −22 °C. (a) Experimental spectrum. (b) Simulated spectrum, A_2B_2 system (PANIC): $\delta(P^A)$ = −279.4 ppm; $\delta(P^B)$ = −284.0 ppm; $^1J(P^A-P^B)$ = 175 Hz; $^1J(Rh-P^A)$ = 33.9 Hz; $^2J(Rh-P^B)$ = 0 Hz; $^2J(P^A-PPh_3)$ = 4.7 Hz; $^3J(P^B-PPh_3)$ = 8.6 Hz; line width = 7 Hz.

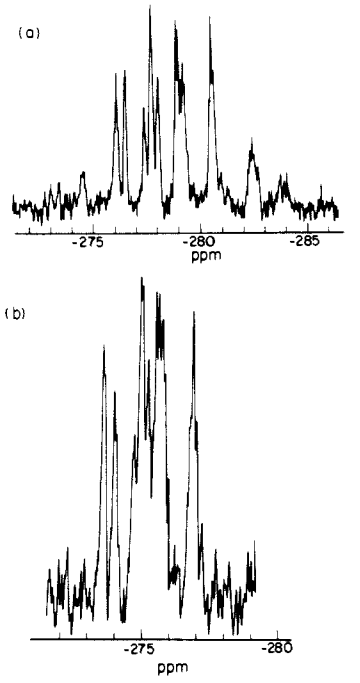

Figure 4. 81.02-MHz $^{31}P\{^1H\}$ NMR spectra in CD_2Cl_2 of P_4 ligand of (a) Complex **2** at −20 °C and (b) Complex **3** at −40 °C.

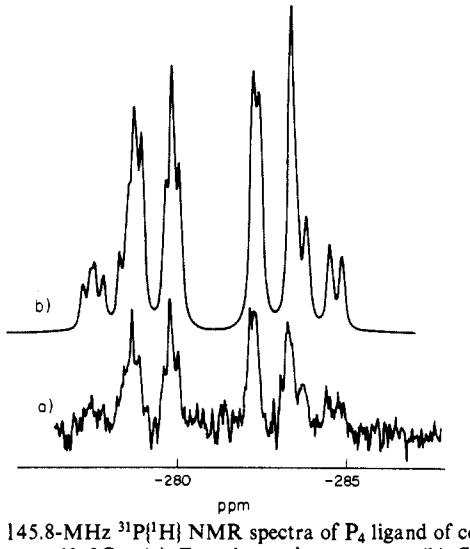

Figure 5. 145.8-MHz $^{31}P\{^1H\}$ NMR spectra of P_4 ligand of complex **1** in CD_2Cl_2 at −60 °C. (a) Experimental spectrum. (b) Simulated spectrum with $\delta(P^A) = -278.8$ ppm; $\delta(P^B) = -283.3$ ppm; $^2J(P^A-P^B) = 175$ Hz; $^2J(P^A-P^X) = 4.7$ Hz; $^3J(P^B-P^X) = 8.6$ Hz; $^1J(Rh-P^A) = 33.9$ Hz; $^2J(Rh-P^B) = 0$ Hz; line width = 20 Hz.

quency, this spectrum confirmed the analysis at 81.02 MHz (Figure 5).

Spectra of **1** over the temperature range −70 to +37 °C and of **2** from −40 to +19 °C show no significant changes in the pattern of P_4 and PPh_3 resonances, although small changes in chemical shifts do occur: e.g., complex **1**, $\delta(P^A)$ −278.3 (−60 °C), −280.2 (26 °C); $\delta(P^B)$ −283.3 (−60 °C), −285.1 (26 °C); $\delta(P^X)$ 43.3 (−60 °C), 42.9 (26 °C); complex **2**: $\delta(P^A)$ −276.0 (−40 °C), −276.9 (19 °C); $\delta(P^B)$ −280.6 (−40 °C), −281.5 (19 °C). Above approximately −20 °C (especially above 0 °C) decomposition of solutions of **1** and **2** sets in, and the intensity of the NMR signal assignable to the P_4 complex decreases; a resonance due to free PPh_3 and a weaker resonance at ca. δ −520, assignable to free P_4, appear and grow in intensity. Also, a broad resonance centered around 30 ppm is observed from solutions of **1** and **2** that have been at ambient temperature for several hours; such solutions exhibited no ESR spectra at ambient temperatures, but on cooling to −140 °C weak signals were observed from the frozen solutions. Spectra of complex **3** were recorded only at −40 °C since even at this temperature resonances assignable to free PPh_3 and P_4 were observed.

The chemical shifts of coordinated PPh_3 groups, $\delta(P^X)$, in complexes **1–3** are at slightly higher frequencies than *trans*-PPh_3 ligands in the complexes $[RhY(PPh_3)_2L]$ (Y = halogen, L = PPh_3, CO, C_2H_4)[41,42] or $[RhCl_2(COR)(PPh_3)_2]$.[41,43] Also, the coupling constants $^1J(Rh-P^X)$ are smaller than in the $[RhY(PPh_3)_2L]$ complexes[42] but greater than in $[RhCl_2(COR)(PPh_3)_2]$[43] or, for *trans*-PPh_3 groups, in Rh(III) complexes *mer*-$[RhCl_3(PR_3)_3]$.[44] However, it may be noted that both $\delta(P^X)$ and $^1J(Rh-P^X)$ values are similar to those of the trans ligands in $[RhH_2Cl(PPh_3)_3]$.[42b] The decrease in $\delta(P^X)$ values with change in halogen in complexes **1–3**, i.e., Cl > Br > I, is comparable to similar trends for complexes $[RhY(PPh_3)_2L]$ (Y = halogen, L = PPh_3, CO).[41,42]

Free P_4 exhibits a very high field resonance which is markedly dependent on solvent and concentration effects;[45] chemical shifts can vary by more than 40 ppm (70 ppm from solid P_4), and in CH_2Cl_2, δ values around −520 to −530 ppm are found. The P_4 groups of complexes **1–3** are deshielded on coordination by approximately 240 ppm relative to free P_4. The chemical shifts increase by small increments with change of halogen ligand, Cl < Br < I. Rather unexpectedly, $\delta(P^A)$ and $\delta(P^B)$ values are very close, although only the two P^A nuclei show coupling to ^{103}Rh and these must be coordinated in an η^2 manner, I, as confirmed by

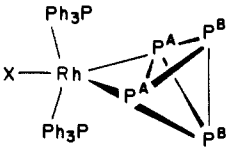

I
complexes 1-3

X-ray diffraction (vide infra). Coupling between ^{103}Rh and P^B is unobservable (<1 Hz), and the values for $^1J(Rh-P^A)$ of 31–34 Hz are significant but small in relation to normal Rh–PR_3 interactions.[41] Low metal–P coupling constants are also found for the side-bonded P_2Ph_2 ligand in $[Pt(\eta^2-P_2Ph_2)(dppe)]$[46] and in η^3-P_3 complexes of Rh and Pt.[47] Of special note are the NMR parameters of $[Rh(\eta^3-P_3)(triphos)]$[18b,47] for which, in CD_2Cl_2 at 29 °C, we find $\delta(\eta^3-P_3)$ −272.0, $^1J(Rh-P)$ = 28.3 Hz, and $^2J(P-P)$ = 12.3 Hz (inappreciable variance with values reported recently by Sacconi et al.:[47] δ −261.0, $^1J(Rh-P)$ = 13 Hz, and $^2J(P-P)$ = 12 Hz).

The $^1J(P^A-P^B)$ values obtained by computer simulation (175–182 Hz) are typical of many one-bond P–P coupling constants between P(III) atoms, but it should be noted that a wide range of $^1J(P-P)$ values have been reported (e.g., −108 to +590 Hz).[48] The couplings between P^X and P^A or P^B nuclei are small and, of these, the $^3J(P^B-P^X)$ values are the largest; this may correspond to more interaction between the P^X and P^B nuclei in the $RhP^X_2P^B_2$ plane, although the X-ray determined structure of

(41) Pregosin, P. S.; Kunz, R. W. In "N.m.r. Basic Principles and Progress"; Diehl, P.; Fluck, E.; Kosfeld, R., Eds.; Springer-Verlag: Berlin, 1979, Vol. 16 and references therein.
(42) (a) Brown, T. H.; Green, P. J. *J. Am. Chem. Soc.* **1970**, *92*, 2359. (b) Tolman, C. A.; Meakin, P. Z.; Lindner, D. L.; Jesson, P. J. *Ibid.* **1974**, *96*, 2762. (c) Garrou, P. E.; Hartwell, G. E. *Inorg. Chem.* **1976**, *15*, 646.
(43) Egglestone, D. L.; Baird, M. C.; Lock, C. J. L.; Turner, G. *J. Chem. Soc., Dalton Trans.* **1977**, 1576. Slack, D. A.; Egglestone, D. L.; Baird, M. C. *J. Organomet. Chem.* **1978**, *146*, 71. Lau, K. S. Y.; Becker, Y.; Huang, F.; Baenziger, N.; Stille, J. K. *J. Am. Chem. Soc.* **1977**, *99*, 5664.
(44) Grim, S. O.; Ference, R. A. *Inorg. Chim. Acta* **1970**, *4*, 277.
(45) Heckmann, G.; Fluck, E. *Z. Naturforsch. B: Anorg. Chem., Org. Chem., Biochem., Biophys., Biol.* **1971**, *26*, 282; **1972**, *27*, 764. Krabbes, G.; Grossmann, G. *Z. Chem.* **1971**, *11*, 470.
(46) Chatt, J.; Hitchcock, P. B.; Pidcock, A.; Warrens, C. P.; Dixon, K. R. *J. Chem. Soc., Chem. Commun.* **1982**, 932.
(47) Di Vaira, M.; Sacconi, L.; Stoppioni, P. *J. Organomet. Chem.* **1983**, *250*, 1983.
(48) Mavel, G. *Annu. Rep. NMR Spectrosc.* **1973**, *5B*, 1.
(49) Bernstein, H. J.; Powling, J. *J. Chem. Phys.* **1950**, *18*, 1018.
(50) Venkateswaran, C. S. *Proc.—Indian Acad. Sci., Sect. A* **1935**, *2*, 260; **1936**, *4*, 345.

Table VI. Vibrational Frequencies (cm^{-1}) of P_4 in the Free Molecule and in the Rhodium-P_4 Complexes[a]

P_4 (free)[b]		assignment[c]		$RhCl(P_4)(PPh_3)_2$		$RhBr(P_4)(PPh_3)_2$		$RhI(P_4)(PPh_3)_2$		$RhCl(P_4)(AsPh_3)_2$		assignment[c]
IR	R	T_d	C_{2v}	IR	R	IR	R	IR	R	IR	R^e	C_{3v}
	606	$\nu_1(A_1) \rightarrow$	A_1	569 s	571 w	571 m	570 w	568 m	568 w	566 s	n.o.	A_1
461	465	$\nu_2(T_2) \rightarrow$	A_1	433 s	438 m	433 s	433 w	432 m	427 w	428 m	436 w	A_1
			B_1	387 m	386 s	384 m	383 s	382 m	380 s	396 m	390 m	E
			B_2	~376 sh	~374 sh	~375 sh	n.o.	n.o.	n.o.			
	363	$\nu_3(E) \rightarrow$	B_1	349 w	344 w	348 w	n.o.	348 w	n.o.	*d*	n.o.	E
			B_2									

[a] Abbreviations: m, medium; s, strong, sh, shoulder, w, weak; n.o. an expected band was not observed. [b] IR of P_4 in CS_2 solution.[49] Raman of liquid phosphorus.[50] [c] The C_{2v} assignments apply to the PPh_3 complexes. The C_{3v} assignments are for the $AsPh_3$ complex. [d] Obscured by ligand absorption. [e] Poor Raman scatter.

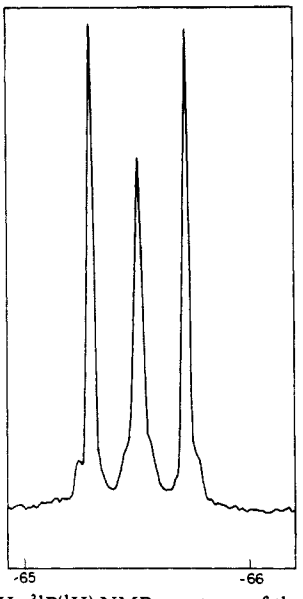

Figure 6. 81.02-MHz $^{31}P\{^1H\}$ NMR spectrum of the P_4 ligand of complex **6** in CD_2Cl_2 at −6 °C (δ = −65.5 ppm).

1 does not indicate close proximity of P^X and P^B.

The $^{31}P\{^1H\}$ NMR spectrum of complex **6** in CD_2Cl_2 at temperatures between −60 and 0 °C comprises a simple triplet with component intensity ratios ca. 3:2:3 (Figure 6). The chemical shift is >200 ppm higher than for P_4 groups in complexes **1**–**3** and shows a slight decrease on raising the temperature: δ −64.1 (−60 °C); −65.5 (−6 °C). The splitting between outer components of the triplet remains essentially constant at 34.1 ± 0.15 Hz over the same temperature range. After standing at 0 °C for 0.5–1 h the triplet resonance disappears and is not regenerated on cooling to −40 °C, but a very weak resonance at δ −190 is observed. Assuming a structure for **6** that is static on the NMR time scale, it is not possible to simulate the observed triplet by using a model based on an A_2B_2 tetraphosphorus ligand coupled to ^{103}Rh and having a significant $^1J(P^A-P^B)$ coupling constant (note: small coupling to ^{75}As may also be present). However, if $\delta(P^A) \simeq \delta(P^B)$ (cf. the small difference between these parameters for complexes **1**–**3**) and if $^1J(P^A-P^B) \simeq 0$ Hz, a 1:2:1 triplet is produced when $^1J(Rh-P^A)$ = 34.1 Hz and $^2J(Rh-P^B)$ = 0 Hz; alternatively a 3:2:3 triplet is produced from an A_3B system with the same parameters—close to that observed experimentally. This latter analysis would be consistent with coordination geometry II. A

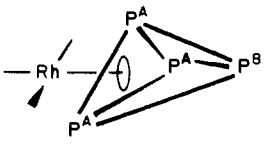

II
complex **6** ?

zero value for $^1J(P-P)$ seems unusual, but such couplings do show marked variations;[48] it should also be noted that coupling between P^A and P^B in a distorted tetrahedral unit can occur via one, two, or three bonds, and variations in the signs of such interactions could produce a resultant coupling of zero.

Simulation of the spectrum of complex **6** as an A_3BX (X = Rh) system with $\delta(P^A) = \delta(P^B)$, $^1J(Rh-P^A)$ = 34.1 Hz, and $^2J(Rh-P^B)$ = 0 Hz gives a triplet similar to that obtained experimentally, provided that $J(P^A-P^B)$ and $J(As-P)$ values are 0 ± 2 Hz. We tentatively propose η^3-coordination for the P_4 ligand in **6**, although confirmation, by X-ray diffraction of a suitable crystal, would be highly desirable.

The $^{31}P\{^1H\}$ NMR spectrum of complex **7** at −40 °C in CD_2Cl_2 comprises a symmetrical resonance assignable to equivalent PPh_3 groups, δ −0.02, and a complex pseudo-quartet of the P_4 group centered at −237.3 ppm. Smaller signals, assumed to arise from decomposition impurities, are present at −91.5 and −3.6 ppm. There is also a small signal due to free PPh_3. At this stage satisfactory analysis of the spectrum has not been achieved.

Vibrational Spectra. Table VI summarizes the infrared and Raman frequencies of the P_4 molecule in the rhodium complexes and compares them with the frequencies of the free P_4 molecule. It is not possible to distinguish between the C_{2v} $Rh(\eta^2-P_4)$ structure of the PPh_3 complexes and the C_{3v} $Rh(\eta^3-P_4)$ structure which we propose for the $AsPh_3$ complex on the basis of the results in Table VI. The frequencies assigned to P_4 in the complexes are from 15 to 90 cm^{-1} lower in energy than the corresponding frequencies in free P_4. The relatively small perturbation of the P_4 vibrational spectrum on binding to rhodium is consistent with the results of the X-ray structure determination and the molecular orbital calculations, which show that only the bound edge of the P_4 molecule is significantly altered.

$[RhCl(CO)(P_4)(AsPh_3)]$ has a strong ν(CO) absorption at 2045 cm^{-1} (CsI disk). The elevated value for this frequency (cf. ν(CO) = 1963 cm^{-1} (CsI disk) for *trans*-$[RhCl(CO)(PPh_3)_2]$) is consistent with describing the P_4 as having undergone oxidative addition to the rhodium. A ν(CO) shoulder at ~1990 cm^{-1} in the P_4 complex may be due to an impurity.

The Solid-State Molecular Structure of $[RhCl(P_4)(PPh_3)_2]$. Molecules of **1** cocrystallize with CH_2Cl_2 solvent (1:2), but there are no serious intermolecular contacts in the lattice. The solvent molecules appear to have quite normal parameters [C–Cl 1.719 (10)–1.762 (8) Å, Cl–C–Cl 111.1 (5)° and 111.4 (4)°].

Figure 7 presents a perspective view of a single molecule of **1** in a projection nearly perpendicular to the best plane through Rh, Cl(1), P(1), and P(2) and demonstrates the atomic numbering scheme. Although the molecule possesses no crystallographically required point symmetry, Figure 7 clearly shows the effective C_2 symmetry that is present. Figure 8 is a similarly oriented view of the rhodium coordination sphere and P_4 ligand; this portion of the complex displays effective C_{2v} point symmetry. Table VII lists the internuclear separations and interbond angles.

The essential result of this structural study is that η^2-bonding of the P_4 ligand to the rhodium center is confirmed. Moreover, the metal-bonded P–P edge lies essentially perpendicular to the coordination plane of the metal atom, as implied by the results of the NMR study.

Complex **1** represents only the second crystallographically authenticated example of the ligation of a transition metal by P_4 and is the only example to date of η^2-coordination of P_4. In $[Ni(\eta^1-P_4)(np)]$[15] the Ni–P_4 distance is 1.99 (1) Å and the P_4 unit

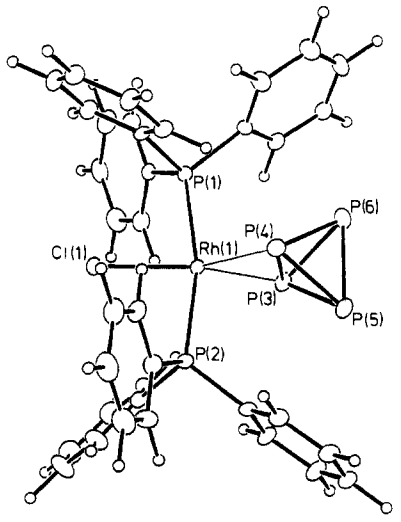

Figure 7. Perspective view of the molecule $[RhCl(P_4)(PPh_3)_2]$. Thermal ellipsoids are drawn at the 50% probability level, except for H atoms, which have an artificial radius of 0.1 Å for clarity.

Table VII. Derived Geometrical Parameters

	Bond Distances, Å		
Rh(1)–Cl(1)	2.4095 (14)	P(3)–P(4)	2.4616 (22)
Rh(1)–P(1)	2.3340 (14)	P(3)–P(5)	2.2163 (22)
Rh(1)–P(2)	2.3312 (14)	P(3)–P(6)	2.2217 (23)
Rh(1)–P(3)	2.3016 (16)	P(4)–P(5)	2.2034 (23)
Rh(1)–P(4)	2.2849 (16)	P(4)–P(6)	2.2085 (23)
P(1)–C(1)	1.836 (4)	P(5)–P(6)	2.1884 (24)
P(1)–C(7)	1.830 (4)	Cl(2)–C(37)	1.747 (10)
P(1)–C(13)	1.827 (4)	Cl(3)–C(37)	1.719 (10)
P(2)–C(19)	1.831 (4)	Cl(4)–C(38)	1.762 (8)
P(2)–C(25)	1.831 (4)	Cl(5)–C(38)	1.728 (8)
P(2)–C(31)	1.837 (4)		
	Bond Angles, deg		
Cl(1)–Rh(1)–P(1)	82.62 (5)	P(5)–P(3)–P(6)	59.09 (7)
Cl(1)–Rh(1)–P(2)	83.56 (5)	Rh(1)–P(4)–P(5)	106.01 (8)
Cl(1)–Rh(1)–P(3)	152.50 (5)	Rh(1)–P(4)–P(6)	105.70 (8)
Cl(1)–Rh(1)–P(4)	142.58 (5)	P(5)–P(4)–P(6)	59.47 (7)
P(1)–Rh(1)–P(2)	166.10 (5)	P(3)–P(5)–P(4)	67.69 (7)
P(1)–Rh(1)–P(3)	96.10 (5)	P(3)–P(5)–P(6)	60.58 (7)
P(1)–Rh(1)–P(4)	96.06 (5)	P(4)–P(5)–P(6)	60.38 (7)
P(2)–Rh(1)–P(3)	96.83 (5)	P(3)–P(6)–P(4)	67.51 (7)
P(2)–Rh(1)–P(4)	94.05 (5)	P(3)–P(6)–P(5)	60.33 (7)
P(3)–Rh(1)–P(4)	64.92 (5)	P(4)–P(6)–P(5)	60.15 (7)
Rh(1)–P(1)–C(1)	121.93 (12)	P(1)–C(1)–C(2)	117.23 (25)
Rh(1)–P(1)–C(1)	107.44 (12)	P(1)–C(1)–C(6)	122.68 (25)
Rh(1)–P(1)–C(13)	112.87 (12)	P(1)–C(7)–C(8)	117.33 (24)
C(1)–P(1)–C(7)	104.69 (16)	P(1)–C(7)–C(12)	122.60 (25)
C(1)–P(1)–C(13)	100.51 (16)	P(1)–C(13)–C(14)	119.2 (3)
C(7)–P(1)–C(13)	108.58 (16)	P(1)–C(13)–C(18)	120.8 (3)
Rh(1)–P(2)–C(19)	120.19 (12)	P(2)–C(19)–C(20)	117.84 (25)
Rh(1)–P(2)–C(25)	112.47 (13)	P(2)–C(19)–C(24)	122.07 (25)
Rh(1)–P(2)–C(31)	109.20 (13)	P(2)–C(25)–C(26)	120.7 (3)
C(19)–P(2)–C(25)	102.18 (17)	P(2)–C(25)–C(30)	119.1 (3)
C(19)–P(2)–C(31)	103.12 (17)	P(2)–C(31)–C(32)	117.4 (3)
C(25)–P(2)–C(31)	108.85 (18)	P(2)–C(31)–C(36)	122.6 (3)
Rh(1)–P(3)–P(5)	105.02 (7)	Cl(2)–C(37)–Cl(3)	111.1 (5)
Rh(1)–P(3)–P(6)	104.70 (8)	Cl(4)–C(38)–Cl(5)	111.4 (4)

is slightly distorted from a regular tetrahedron (of dimension 2.21 Å), with P–P distances involving the coordinated atom somewhat elongated [2.20 (3) vs. 2.09 (3) Å]. As we have already pointed out, examples of Rh–(η^3-P_3) fragments are known; in [Rh(η^3-P_3)(triphos)][11] Rh–P_3 is 2.418 (2) Å and P–P 2.152 (2) Å, while in $[RhM'(triphos)(\mu\text{-}\eta^3\text{-}P_3)]^{2+}$ (M' = Co, Ni) the distances between P_3 and (disordered) metal atoms span the ranges 2.294 (10)–2.337 (9) Å (M' = Co) and 2.311 (5)–2.558 (5) Å (M' = Ni), complemented by P–P in the range 2.147 (6)–2.315 (6) Å.[12] In **1** the Rh–P_4 distances are 2.3016 (16) and 2.2849 (16) Å; P–P bond lengths fall into three apparent catagories—the metal-bonded edge is substantially the longest, 2.4616 (22) Å, while the opposite

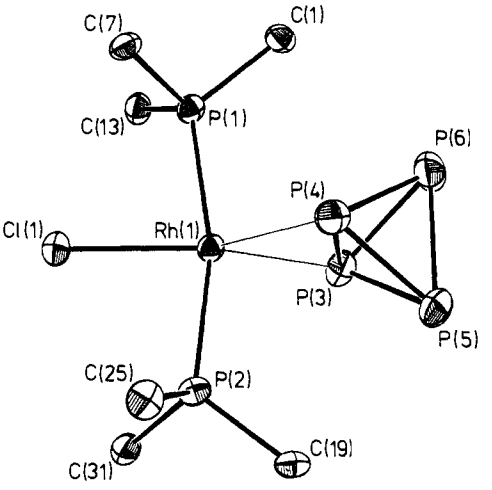

Figure 8. Central part of $[RhCl(P_4)(PPh_3)_2]$.

edge is significantly the shortest, 2.1884 (24) Å. Between these extremes, although much closer to the latter, are the remaining P–P distances, 2.2034 (23)–2.2217 (23) Å.

The coordination geometry at the Rh atom is essentially trans square planar if the P_4 ligand is assumed to occupy one coordination site. Employing the midpoint (mp) of the P(3)–P(4) bond, we find the the rms deviation from planarity of the fragment RhCl(1)P(1)P(2)(mp) is 0.034 Å. A number of analogous complexes of the general form *trans*-$[RhCl(L)(PR_3)_2]$ (L = two-electron ligand) have been structurally studied.[51] The Rh–Cl bond length in **1**, 2.4095 (14) Å, lies at the upper extreme of the range previously established [2.356 (1)–2.405 (1) Å], implying a substantial trans influence of the η^2-P_4 ligand. By comparison with those analogues containing bis(triphenylphosphine),[51a-e] the cis influence of η^2-P_4 appears to be comparable to that of η^1-CS, η^1-CO, and PPh_3.

There has recently been some conjecture[52] about the relative thermodynamic stabilites of η^1-, η^2-, and η^3-bonding of the P_4 ligand to the fragment $[RhCl(PH_3)_2]$. Following our initial study[18c] of the bonding within the model complex *trans*-$[RhCl(P_4)(PH_3)_2]$, Albright and co-workers found, using geometry-optimized EHMO calculations, that in this complex the η^1 mode is significantly more stable than the η^2 mode if the P_4 ligand retains its T_d geometry but that allowing distortion of the P_4 ligand by elongation of the metal-bonded edge stabilizes the η^2 with respect to the η^1 mode. The final geometry-optimized energy for the η^2 structure was calculated to be 15 kcal/mol more stable than the optimized η^1 structure. However, the calculated elongation of the metal-bonded P_4 edge and the calculated Rh–P distance were both much greater than found in the structure of **1**.

Geometry optimization calculations on the model complex $[RhCl(P_4)(PH_3)_2]$ do not take into account the possible effects of intramolecular steric crowding on the structure of **1**. Figure 9 shows a space-filling representation of the molecule of **1**. From this it may be seen that the η^2- bonded P_4 ligand fills a wedge-

(51) (a) L = CO, R = Ph. Triclinic form; Del Pra, A.; Zanotti, G.; Segala, P. *Cryst. Struct. Commun.* **1979**, *8*, 959. Monoclinic form; Ceriotti, A.; Ciani, G.; Sirioni, A. *J. Organomet. Chem.* **1983**, *247*, 345. (b) L = CS, R = Ph. De Boer, J. L.; Rogers, D.; Skapski, A. C.; Troughton, P. G. H. *J. Chem. Soc., Chem. Commun.* **1966**, 756. (c) L = η^2-C_2F_4, R = Ph. Hitchcock, P. B.; McPartlin, M.; Mason, R. *J. Chem. Soc., Chem. Commun.* **1969**, 1367. (d) L = PPh_3, R = Ph. Red form: Hitchcock, P. B.; McPartlin, M.; Mason, R. *J. Chem. Soc., Chem. Commun.* **1969**, 1367; Bennett, M. J.; Donaldson, P. B. *Inorg. Chem.* **1977**, *16*, 655. Orange form: Bennett, M. J.; Donaldson, P. B. *Inorg. Chem.* **1977**, *16*, 655. (e) L = η^2-[(*t*-$Bu_2OC_6H_2C)_2$]$_2$, R = Ph. Hagelee, L.; West, R.; Calabrese, J.; Norman, J. *J. Am. Chem. Soc.* **1979**, *101*, 4888. (f) L = η^2-C_2H_4. R = *i*-Pr. Busetto, C.; D'Alfonso, A.; Maspero, F.; Perego, G.; Zazzetta, A. *J. Chem. Soc., Dalton Trans.* **1977**, 1828. (g) L = η^1-N_2, R = *i*-Pr. Thorn, D. L.; Tulip, T. H.; Ibers, J. A. *J. Chem. Soc., Dalton Trans.* **1979**, 2022. (h) L = CO, $(PR_3)_2$ = $Ph_2CH_2C_{18}H_{10}CH_2PPh_2$. Bachechi, F.; Zambonelli, L.; Venanzi, L. M. *Helv. Chim. Acta* **1977**, *60*, 2815.

(52) Kang, S.-K.; Albright, T. A.; Silvestre, J. *Croat. Chem. Acta* **1984**, *57*, 1355.

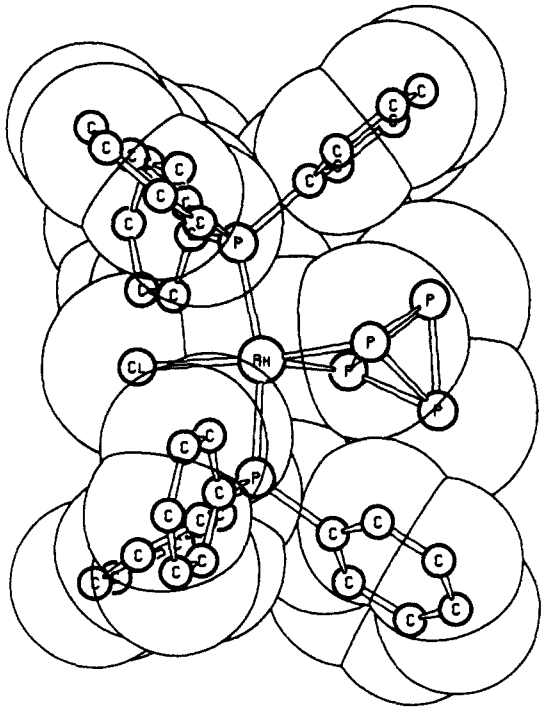

Figure 9. Space-filling diagram of $[RhCl(P_4)(PPh_3)_2]$.

shaped cavity defined by the metal atom, P(1), P(2), and the phenyl rings C(1)–C(6) and C(19)–C(24). The planes defined by the phenyl rings subtend a dihedral angle of 71.60°, which is very close to the interfacial angle of a regular tetrahedron (70.53°), and, indeed, the two P_3 faces containing the metal-bonded edge are each almost parallel to the adjacent phenyl ring (dihedral angles of 15.01° [P(3)P(4)P(6)/C(1)–C(6)] and 2.02° [P(3)P(4)P(5)/C(19)–C(24)]). However, angular distortions of the phosphine ligands have clearly occurred in order to accommodate the η^2-P_4 ligand. Both phosphine groups are substantially bent toward Cl(1), P–Rh–Cl(1) = 82.62 (5)° and 83.56 (5)°, and, in addition, the angles Rh–P–C(1,19) are widened to 121.19 (12)° and 120.19 (12)°, respectively; cf. other Rh–P–C angles between 107° and 113°.

The ⊥ conformation of the P(3)–P(4) edge relative to the rhodium coordination plane in **1** bears comparison with that in *trans*-$[RhCl(ene)(PR_3)_2]$ analogues.[51c,e,f] Furthermore, since C=C bond lengthening as a function of η^2-coordination of alkenes in organometallic complexes is a very well established and understood phenomenon,[53] the observed relative lengthening of P(3)–P(4) in **1** appears to strengthen the analogy between η^2-P_4 and η^2-alkene. This analogy, as well as that between the η^2-P_4 complex and η^2-S_2 complexes of Rh and Ir, is explored in greater detail in the sections describing the electronic structure of an η^2-P_4 complex.

Electronic Structure of $[RhCl(\eta^2\text{-}P_4)(PH_3)_2]$ by EHMO Calculations. In the axial system used here, x and y are interchanged relative to those previously communicated[18c] to facilitate comparison with the results of the following SCF–Xα calculations. Thus the T-shaped $RhClP_2$ fragment (involving PH_3 P atoms) lies in the xz plane. In the ⊥ η^2-P_4 conformation the coordinated P–P edge is parallel to the y axis at positive z.

Figure 10 is a simplified EHMO interaction diagram for the fragments $RhCl(PH_3)_2$ and P_4 to give $[RhCl(P_4)(PH_3)_2]$ in a ⊥ η^2 conformation. The metal fragment and ultimate complex both belong to the C_{2v} point group. Although the P_4 molecule was used with full T_d symmetry, for consistency its orbitals are labeled in Figure 10 in only C_{2v} symmetry; in parentheses are identified the appropriate fully symmetric representations.

(53) See, for example: Mingos, D. M. P. In 'Comprehensive Organometallic Chemistry'; Able, E. W.; Stone, F. G. A.; Wilkinson, G., Eds.; Pergamon: Oxford, England, 1982, Vol. 3, pp 47–58.

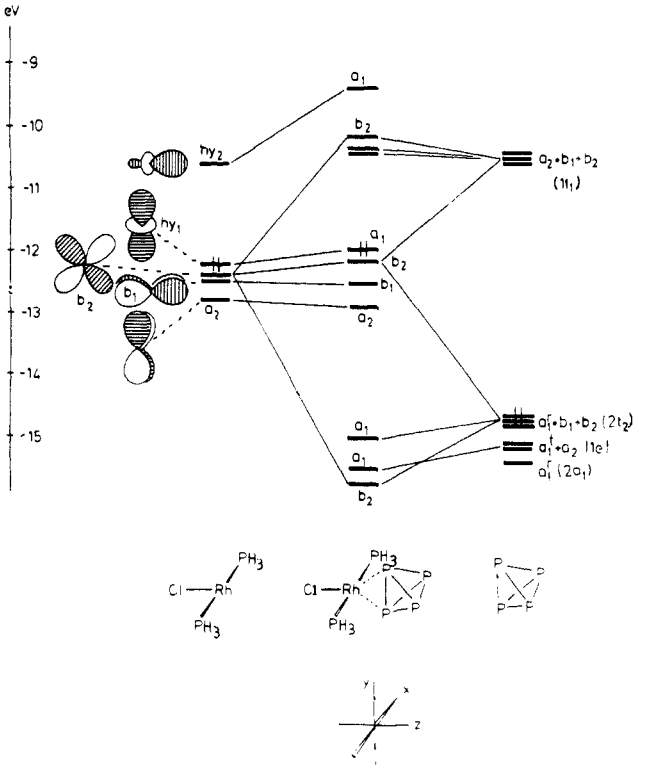

Figure 10. Interaction diagram (EHMO calculations) for the molecule $[RhCl(P_4)(PH_3)_2]$. Note that some occupied molecular orbitals are omitted for the sake of clarity.

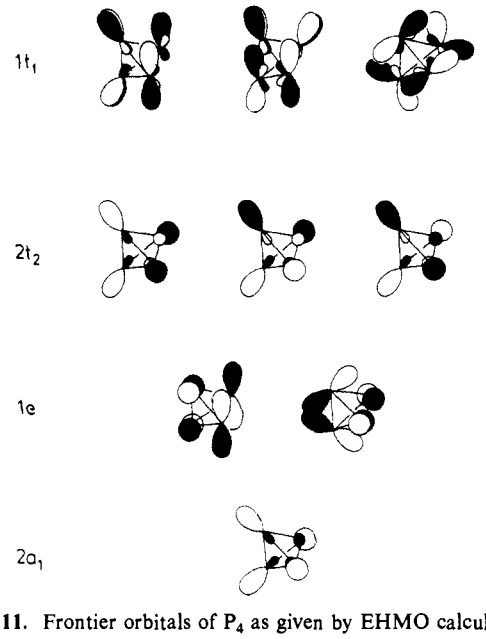

Figure 11. Frontier orbitals of P_4 as given by EHMO calculation.

The P_4 Molecule. The molecular orbitals of tetrahedral P_4 are well-known.[2-9] Our EHMO calculation shows four low-lying MO's ($1a_1 + 1t_2$, of s and sp character, respectively) whose energies are too well removed from those of transition-metal valence orbitals to be of significance in metal–P_4 bonding. The six highest lying occupied MO's of P_4 span the representations (decreasing stability) $2a_1$, 1e, and $2t_2$, while the LUMO is the triply degenerate $1t_1$. Figure 11 sketches the orbitals $2a_1$–$1t_1$.

$2a_1$ is an sp hybrid whose lobes radiate out from the polyhedral center, and thus it is denoted a_1^r. The 1e pair in C_{2v} transform as $a_1 + a_2$ and are derived almost exclusively from 3p atomic orbitals tangential to the polyhedral surface. Thus the a_1 component is labeled a_1^t. The $2t_2$ set, sp hybrid orbitals, transform as $a_1^r + b_1 + b_2$ and the $1t_1$ set as $a_2 + b_1 + b_2$. We find that the HOMO($2t_2$)–LUMO($1t_1$) gap is ca. 4.2 eV and that the

vacant $1t_1$ orbitals are fairly equal dp hybrids. The P–P overlap population is 0.755.

The *trans*-RhCl(PH_3)$_2$ Fragment. T-shaped 14-e d^8 metal fragments are ubiquitous in transition-metal chemistry, occurring in such important complexes as Zeise's salt, Vaska's complex, and Wilkinson's catalyst. The fragment orbitals of *trans*-RhCl(PH_3)$_2$ are well-known.[54] In Figure 10 the LUMO (hy_2, of a_1 symmetry) is a $d_{z^2}/d_{x^2-y^2}/s/p_z$ hybrid orbital directed toward the vacant coordination site and is thus the σ-acceptor orbital of the fragment. Of the band of occupied metal d orbitals, a_1 (hy_1) is localized along the y axis and a_2 (the d_{xy} orbital) lies in the xy plane. Thus, only b_2 (d_{yz}) and b_1 (d_{xz}) are properly oriented for π-donation to suitable orbitals of the fourth ligand in a square-planar complex. The Rh–P and Rh–Cl overlap populations in RhCl(PH_3)$_2$ are 0.708 and 0.302, respectively.

The [RhCl(η^2-P_4)(PH_3)$_2$] Molecule. The interaction diagram for RhCl(PH_3)$_2$ with $\perp$ η^2-P_4 is fairly straightforward. The occupied a_1, b_1, and a_2 metal orbtials are essentially nonbonding in the complex, as expected, and of these a_1 is the HOMO of the complex. The hy_2 orbital stabilizes both a_1^r (from $2t_2$) and a_1^l (from 1e). In the former case the energy separation is less but so is the directed overlap, whereas in the latter case both are greater. The occupied b_2 metal orbital enters into a three-orbital–four-electron interaction with occupied and unoccupied b_2 ligand orbitals, the lowest MO being strongly bonding, the intermediate MO essentially nonbonding, and the highest MO antibonding, between Rh and P_4, although in the last case the antibonding character is somewhat reduced by mixing in of a significant degree of Rh $5p_y$ character.

All other P_4 MO's are in essence nonbonding in the complex and are excluded from the central stack of MO's in Figure 10 for the sake of clarity. The LUMO in the complex is derived from a_2 ($1t_1$), and the HOMO–LUMO gap is ca. 1.7 eV. Computed Rh–PH_3 and Rh–Cl overlap populations are 0.530 and 0.240, respectively. We calculate that the complex is stable with respect to RhCl(PH_3)$_2$ and P_4 by ca. 2.0 eV and that upon coordination a net charge of 1.34 e is transferred from the metal fragment to the P_4 unit.

We undertook the EHMO study to explore the apparent similarity between η^2-coordination of P_4 and η^2-coordination of an alkene to a transition-metal fragment like RhCl(PH_3)$_2$. The latter is classically described by the Dewar–Chatt–Duncanson (D–C–D) bonding model,[55] in which σ-donation from an alkene π to a metal acceptor orbital is complemented in a synergic manner by π back-donation from an occupied metal orbital to the unoccupied ligand π^* orbital. For η^2-bonded P_4 the a_1 interaction of Figure 10 clearly corresponds to the σ component of the D–C–D model, but now the π component is a three-orbital–four-electron interaction rather than the two-orbital–two-electron one of a coordinated alkene. Whether η^2-ene or η^2-P_4, both components of the overall bonding weaken the coordinated link. In III, computed

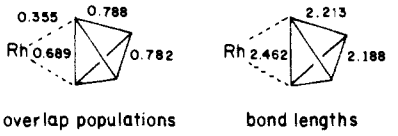

III

overlap populations for the $\perp$ η^2-P_4 unit are compared with the appropriate average crystallographically observed bond lengths. Within the P_4 unit the metal-bonded edge is clearly the weakest.

Rotation of the P_4 ligand about the z axis from $\perp$ to $\parallel$ conformation has a dramatic effect on the interatomic overlap populations and the total energy of the complex. In the $\parallel$ η^2-conformation the P_4 ligand competes with the PH_3 ligands for π bonding from the Rh $4d_{xz}$ orbital (b_1 symmetry), leaving the d_{yz} orbital nonbonding. This results in substantially weaker Rh–PH_3 and Rh–P_4 bonding (overlap populations Rh–PH_3 0.350, Rh–P_4 0.129; cf. Rh–P_4 in $\perp$ mode 0.355), although, as expected, the coordinated P–P edge is now not so much weakened (overlap population 0.704), and the Rh–Cl bond, whose strength reflects changes in the σ component of the Rh–P_4 bonding, is hardly altered (overlap population 0.248). Upon rigid rotation of the P_4 unit (about the z axis) from the $\perp$ conformation, a single maximum in the energy profile is reached at $\pi/2$, thus corresponding to the $\parallel$ conformation. This is ca. 5 eV less stable than the $\perp$ form and thus is predicted to be unstable with respect to RhCl(PH_3)$_2$ and P_4. It should be noted that this rotation barrier is several times larger than that computed for analogous metal–alkene complexes.[53]

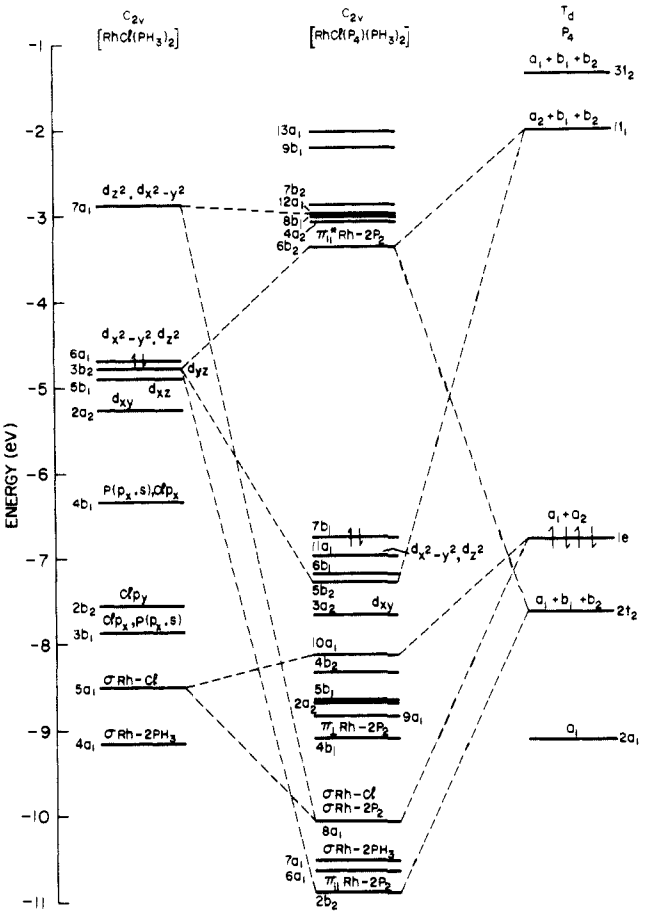

Figure 12. SCF–Xα valence energy levels for [RhCl(P_4)(PH_3)$_2$], [RhCl(PH_3)$_2$], and P_4 above −11 eV. PH_3 P–H bonding orbitals have been omitted from the diagram. Paired arrows mark the highest occupied levels. The Rh–P_4 bonding orbitals are designated as $\pi_\parallel$ Rh–2P2, $\pi_\perp$ Rh–2P2, and σ Rh–2P2 to indicate respectively in-plane pi, out-of-plane pi, and sigma interactions. The C_{2v} representations for the T_d P_4 orbitals are given above each level. The important interactions between the orbitals of the P_4 molecule and those of the [RhCl(PH_3)$_2$] fragment which give rise to the major Rh–P_4 bonding orbitals in the complex are shown by the connecting lines.

Electronic Structure of [RhCl(η^2-P_4)(PH_3)$_2$] by Xα–SW Calculations. The calculated ground-state one-electron energies, charge distributions, and partial wave analyses for the valence molecular orbitals of [RhCl(P_4)(PH_3)$_2$] are summarized in Table VIII; the basis function notation is explained in Table IX. Figure 12 is a diagram of the valence energy levels which also shows the levels calculated for the RhCl(PH_3)$_2$ fragment and for the P_4 molecule.[56,57] Table X gives the calculated total charge distribution as well as estimated net atomic charges, while Table XI

(54) Hoffmann, R. *Angew. Chem., Int. Ed. Engl.* **1982**, *21*, 711.
(55) Dewar, M. J. S. *Bull. Soc. Chim. Fr.* **1951**, *18*, C79. Chatt, J.; Duncanson, L. A. *J. Chem. Soc.* **1953**, 2939.
(56) The RhCl(PH_3)$_2$ fragment was assumed to have the same geometry and bond distances as in the P_4 complex. Overlapping atomic-sphere radii were taken as 89% of the atomic number radii.
(57) The P_4 molecule was calculated under T_d symmetry with P–P distances of 2.21 Å and P–P–P angles of 60°. Overlapping atomic-sphere radii were 89% of the atomic number radii.

Table VIII. Valence Molecular Orbitals of $[RhCl(P_4)(PH_3)_2]$

		charge distribution, %[b]									basis functions[c]		
level[a]	energy, eV	Rh	Cl	2P1	2P2	2P3	2H1	4H2	INT	OUT	Rh	2P2	2P3
13a1	−2.015	5	0	1	18	19	0	0	50	7			
9b1	−2.213	1	0	2	15	27	0	0	49	6			
7b2	−2.896	3	0	1	21	29	0	1	41	3		$\pi^*_{\parallel}$, $s\sigma^*$	$\pi_\perp$
12a1	−2.995	37	10	21	9	2	1	3	15	2	d_{z^2}, $d_{x^2-y^2}$		
8b1	−3.017	1	0	1	19	51	0	0	27	1		$\pi_\perp$	$\pi^*_{\parallel}$, $p\sigma^*$
4a2	−3.081	3	0	0	31	38	0	0	26	1		$\pi^*_\perp$	$\pi^*_\perp$
6b2	−3.372	20	1	1	44	2	0	0	30	1	d_{yz}, p_y	$p\sigma^*$, $\pi^*_{\parallel}$	
7b1	−6.760	31	0	30	5	15	3	2	13	0	d_{xz}, p_x		$\pi^*_{\parallel}$
11a1	−6.970	62	11	2	4	5	0	0	14	0	$d_{x^2-y^2}$, d_{z^2}		
6b1	−7.188	25	44	16	1	1	1	2	10	1	d_{xz}		
5b2	−7.288	30	21	0	25	11	0	0	12	0	d_{yz}	$p\sigma^*$, $s\sigma^*$	$\pi_\perp$
3a2	−7.665	69	0	2	7	11	0	2	9	0	d_{xy}		$\pi^*_\perp$
10a1	−8.138	11	25	2	31	18	1	0	13	1	p_z, s, $d_{x^2-y^2}$, d_{z^2}	$\pi_{\parallel}$, $p\sigma$	$\pi_{\parallel}$, $p\sigma$
4b2	−8.344	8	61	1	8	5	0	1	15	0			
5b1	−8.687	8	31	17	10	14	0	5	15	0			$\pi^*_{\parallel}$, $s\sigma^*$, $p\sigma^*$
2a2	−8.689	14	0	1	39	27	0	2	16	0	d_{xy}	$\pi^*_\perp$	$\pi^*_\perp$
9a1	−8.842	2	15	2	11	55	1	1	13	0		$p\sigma$	$p\sigma$, $\pi_{\parallel}$
4b1	−9.108	27	8	5	20	22	4	3	11	0	d_{xz}	$\pi_\perp$	$\pi^*_{\parallel}$, $s\sigma^*$, $p\sigma^*$
8a1	−10.080	27	23	10	20	7	1	2	9	1	d_{z^2}, $d_{x^2-y^2}$, s	$p\sigma$, $\pi_{\parallel}$, $s\sigma$	
7a1	−10.519	42	2	28	13	1	9	1	5	0	d_{z^2}, $d_{x^2-y^2}$	$p\sigma$, $s\sigma$	
6a1	−10.637	11	1	16	21	29	8	8	6	0	$d_{x^2-y^2}$, d_{z^2}	$p\sigma$, $\pi_{\parallel}$, $s\sigma$	$\pi_{\parallel}$, $p\sigma$, $s\sigma$
3b2	−10.658	1	1	46	0	0	0	52	0	1			
1a2	−10.708	2	0	46	0	0	0	51	0	0			
5a1	−10.824	1	1	31	11	18	22	13	3	0		$p\sigma$, $\pi_{\parallel}$	$p\sigma$, $\pi_{\parallel}$, $s\sigma$
3b1	−10.865	4	2	44	1	1	33	15	0	0			
2b2	−10.888	30	1	0	41	21	0	0	6	0	d_{yz}	$\pi^*_{\parallel}$	$\pi_\perp$
2b1	−15.030	0	0	0	15	75	0	0	10	0		$\pi_\perp$	$s\sigma^*$
4a1	−15.335	8	0	0	47	37	0	0	7	0		$s\sigma$, $\pi_{\parallel}$	$s\sigma$, $\pi_{\parallel}$
1b2	−16.322	3	0	0	75	15	0	0	7	0		$s\sigma^*$	$\pi_\perp$
1b1	−12.181	1	0	65	0	0	12	22	0	0			
3a1	−17.275	2	1	65	0	0	11	21	0	0			
2a1	−19.862	2	93	0	0	0	0	0	4	0			
1a1	−22.527	1	0	0	42	57	0	0	0	0		$s\sigma$, $p\sigma$	$s\sigma$, $p\sigma$

[a] The highest occupied level is $7b_1$. [b] Percentage of the total population of the level located within the indicated region (see Figure 1 for the atom numbering scheme); INT refers to the intersphere region and OUT to the extramolecular region. [c] When more than 10% of the population of a level is located within the Rh, 2P2, or 2P3 spheres, the spherical harmonic basis functions contributing more than 10% of the charge in that region are listed in order of decreasing importance. The P2 and P3 d contributions are not shown; they are $8b_1$, 12% P3 d; $4a_2$, 12% P2 d; $5b_2$, 11% P2 d; $10a_1$, 11% P3 d; $2b_2$, 14% P3 d; $2b_1$, 25% P2 d; and $1b_2$, 30% P3 d.

Table IX. Rh, 2P2, and 2P3 Spherical Harmonic Basis Functions for C_{2v} $[RhCl(P_4)(PH_3)_2]$[a,b]

representation	Rh	2P2	2P3
A1	s, p_z, d_{z^2}, $d_{x^2-y^2}$	$s\sigma$, $p\sigma$, $\pi_{\parallel}$	$s\sigma$, $p\sigma$, $\pi_{\parallel}$
A2	d_{xy}	$\pi^*_\perp$	$\pi^*_\perp$
B_1	p_z, d_{xz}	$\pi_\perp$	$s\sigma^*$, $p\sigma^*$, $\pi^*_{\parallel}$
B2	p_y, d_{yz}	$s\sigma^*$, $p\sigma^*$, $\pi^*_{\parallel}$	$\pi_\perp$

[a] See Figure 1 for the P atom numbering scheme. [b] In the symbols for the 2P2 and 2P3 basis functions, superscript * designates an antibonding contribution while subscripts $\parallel$ and $\perp$ indicate respectively that the orbital has its nodal plane perpendicular and parallel to the molecular symmetry plane in which the atoms lie.

Table X. Total Sphere Charges and Approximate Net Atomic Charges for $[RhCl(P_4)(PH_3)_2]$ and $[RhCl(PH_3)_2]$

	$[RhCl(P_4)(PH_3)_2]$			C_{2v} $RhCl(PH_3)_2$		
sphere	total charge	normalized total charge[a]	net charge[b]	total charge	normalized total charge[a]	net charge[b]
Rh	44.44	45.45	−0.45	44.58	45.45	−0.45
Cl	16.82	17.65	−0.65	16.80	17.42	−0.42
P1	14.30	14.47	+0.53	14.29	14.42	+0.58
P2	14.46	14.90	+0.10			
P3	14.45	14.91	+0.09			
H1	1.05	1.08	−0.08	1.04	1.06	−0.06
H2	1.02	1.04	−0.04	1.03	1.04	−0.04
INT	3.98			1.72		
OUT	0.16			0.11		

[a] The normalized total charge is obtained by assigning the intrasphere and extramolecular charge in each MO to the atomic spheres in proportion to their contribution to the MO and then summing the atomic-sphere charges over all of the occupied MO's. [b] Net atomic charge = atomic no. − normalized total charge.

gives approximate orbital occupancy values.

The occupied valence molecular orbitals of $[RhCl(P_4)(PH_3)_2]$ have energies in the range −22.5 to −6.8 eV. In general, the ligand and metal orbitals are extensively mixed in the MO's, and it is not possible to identify a set of five predominantly 4d orbitals as would be expected in a ligand-field model of the complex. Levels $11a_1$ and $3a_2$, which may be described respectively as mainly Rh $4d_{x^2-y^2}$, $4d_{z^2}$ hybrid lone pair and mainly Rh $4d_{xy}$ lone pair in character, come the closest to being ligand-field-type metal orbitals.

Examination of Table VIII and Figure 12 suggests that the occupied valence-level MO's may be divided into four more or less well defined groups. First, between −6.75 and −7.75 eV, we find a group of five orbitals, $7b_1$, $11a_1$, $6b_1$, $5b_2$, and $3a_2$, which have large metal atom components and are derived from the five highest lying occupied fragment orbitals (Figure 12). This group includes the HOMO, level $7b_1$, which has the major part of its charge divided equally between a Rh $4d_{xz}$, $5p_x$ hybrid and a PH_3 $3p_x$, $3p_z$, 3s hybrid; it is weakly Rh–PH_3 bonding. The two predominantly metal atom orbitals, $11a_1$ and $3a_2$, which have already been discussed, are also in this group. The remaining two orbitals in the group, $6b_1$ and $5b_2$, both have significant Cl charge but no Rh–Cl interaction. Likewise, the 2P3 charge in level $5b_2$ does not interact with the Rh. Next, between −8 and −9 eV, we have a group of five orbitals, $10a_1$, $4b_2$, $5b_1$, $2a_2$, and $9a_1$, which have only small metal atom components. Two of these, $2a_2$ and $9a_1$, are predominantly P_4 orbitals while one, $4b_2$, is mainly a Cl $3p_y$ lone pair. The remaining two orbitals in the group, $10a_1$ and $5b_1$, have both Cl lone-pair and P_4 character. Continuing to lower energy we find all of the important metal–ligand bonding orbitals ($4b_1$, $8a_1$, $7a_1$, and $2b_2$) in the interval between −9 and −11 eV. The other orbitals in this energy range are either P–P ($6a_1$) or

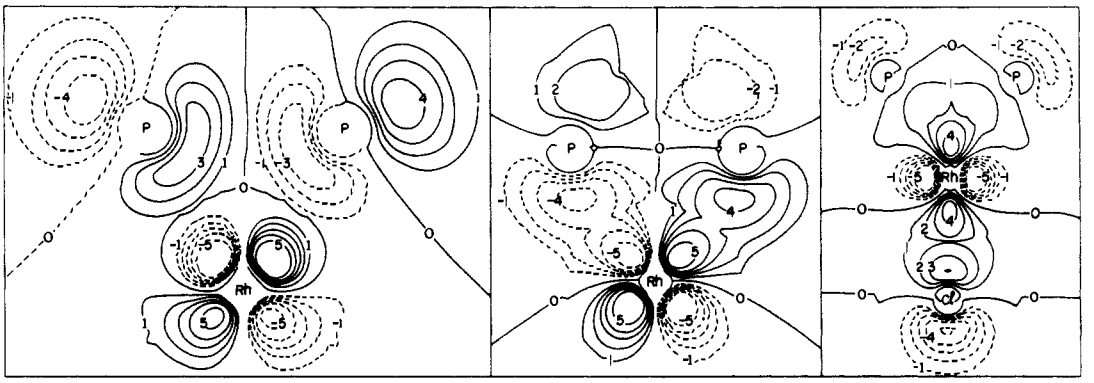

Figure 13. SCF-Xα wave function contour maps of important $[RhCl(P_4)(PH_3)_2]$ orbitals in the yz plane. Solid and broken lines denote contours of opposite sign having magnitudes indicated by the numerical labels: 0, 1, 2, 3, 4, 5 = 0, 0.05, 0.075, 0.10, 0.125, 0.16 $(e/bohr^3)^{1/2}$, respectively. Contours close to atomic centers are omitted for clarity. (a) The LUMO, level $6b_2$. (b) Level $2b_2$, the in-plane Rh–2P2 π-bonding orbital. (c) Level $8a_1$, the σ Rh–2P2 and σ Rh–Cl bonding orbital.

Table XI. Approximate Assignment of Valence Electrons to Rh, 2P2, and 2P3 Basis Functions[a,b,c]

basis function	C_{2v} $RhCl(P_4)(PH_3)_2$		C_{2v} $RhCl(PH_3)_2$
Rh 4d	8.55		8.72
Rh 5p	0.47		0.38
Rh 5s	0.42		0.34
2P2 sσ	1.64	net sσ = −0.07	
2P2 sσ*	1.71		
2P2 pσ	1.36	net pσ = 0.80	
2P2 pσ*	0.56		
2P2 $\pi_\parallel$	1.02	net π = 0.10	
2P2 $\pi_\perp$	0.96		
2P2 $\pi^*_\parallel$	0.86		
2P2 $\pi^*_\perp$	1.02		
2P2 d	0.66		
2P3 sσ	1.70	net sσ = −0.03	
2P3 sσ*	1.73		
2P3 pσ	1.81	net pσ = 1.62	
2P3 pσ*	0.19		
2P3 $\pi_\parallel$	1.10	net π = 0.34	
2P3 $\pi_\perp$	0.96		
2P3 $\pi^*_\parallel$	0.90		
2P3 $\pi^*_\perp$	0.82		
2P3 d	0.6		

[a] See Table IX for basis function notation. [b] The values in this table are the contributions of each of the spherical harmonic basis functions to the total valence charge: total valence charge due to BF = $\Sigma_{\text{valence levels}}$ (normalized atomic-sphere charge for level) X (fraction of sphere charge due to BF). [c] Net π- and σ-electron counts given for 2P2 and 2P3 are the differences between the occupancies of the bonding and antibonding basis functions.

P–H ($3b_2$, $1a_2$, $5a_1$, $3b_1$) bonding. Finally, the fourth group of valence-level MO's occurs between −15 and −23 eV and contains the orbitals with predominantly P–P sσ or sσ* character.

In addition to the occupied orbitals, Table VIII and Figure 12 show a number of virtual levels. The most important of these is the LUMO, level $6b_2$, which is Rh–P_4 in-plane π antibonding in character (cf. Figure 13a) due to interaction between a Rh d_{yz}, p_y hybrid and a pσ*, $\pi^*_\parallel$ hybrid on 2P2. Several of the other virtual levels are also important in interpreting the optical spectrum of the P_4 complex (vide infra).

M–P_4 Bonding. Examination of contour maps shows that the most important contribution to the Rh–P_4 covalent bond comes from the in-plane π interaction in orbital $2b_2$, with a much less important contribution from the σ overlap in orbital $8a_1$. Figure 13b,c shows contour maps of these orbitals. There is also an out-of-plane Rh–P_4 π interaction in orbital $4b_1$, but it is very weak and will not be discussed further.

The $\pi_\parallel$ Rh–2P2 interaction in orbital $2b_2$ of the complex is due to overlap of Rh $4d_{yz}$ with 2P2 $\pi^*_\parallel$. As indicated in Figure 12, level $2b_2$ may be viewed as arising from overlap of the occupied $3b_2$ orbital of an $RhCl(PH_3)_2$ fragment with the b_2 components

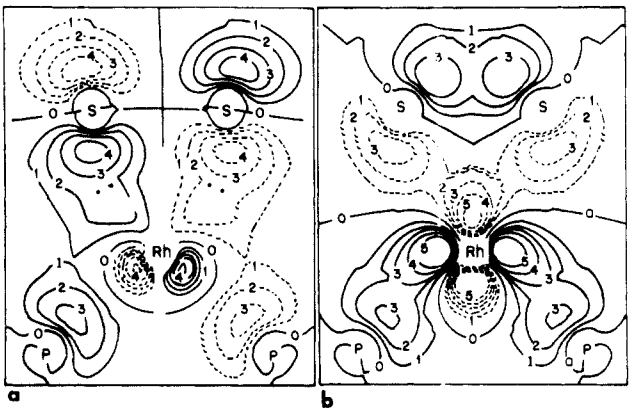

Figure 14. $[Rh(S_2)(PH_3)_4]^+$ wave function contour maps (from ref 59). Contour magnitudes and sign convention are as in Figure 13. (a) The Rh–S_2 in-plane π-bonding orbital (compare with Figure 13b). (b) The Rh–S_2 σ-bonding orbital (compare with Figure 13c).

of the empty $1t_1$ and occupied $2t_2$ orbitals of P_4. This interaction produces the Rh–2P2 bonding and antibonding orbitals, $2b_2$ and $6b_2$, as well as a nonbonding orbital, $5b_2$. The σ Rh–2P2 interaction in level $8a_1$ of the P_4 complex comes from overlap of a Rh ($4d_{z^2}$, $4d_{x^2-y^2}$,5s) hybrid orbital with a (pσ, $\pi_\parallel$, sσ) hybrid on 2P2. An Rh–Cl σ interaction due to overlap of the metal hybrid orbital with Cl p_z is also present in level $8a_1$. In terms of interaction of an $RhCl(PH_3)_2$ fragment with a P_4 molecule (Figure 12), orbital $8a_1$ may be described as arising from overlap of the empty $7a_1$ and filled $5a_1$ fragment orbitals with the a_1 component of the filled 1e orbital on P_4. This interaction produces the Rh–2P2, Rh–Cl σ-bonding orbital $8a_1$ as well as an occupied nonbonding orbital $10a_1$ and the virtual antibonding orbital $12a_1$.[58]

It is interesting to compare the Rh–P_4 bonding in $[RhCl(P_4)(PH_3)_2]$ with what was found by an SCF-Xα analysis for the Rh–S_2 bond in $[Rh(S_2)(PH_3)_4]^+$.[59] In the latter complex the coordination is octahedral, and the edgewise-bonded S_2 group is trans to two PH_3 groups and cis to the other two PH_3 groups. As in the case of the Rh–P_4 bond, the Rh–S_2 bond was found to reside predominantly in two orbitals. In one of these there is an in-plane π overlap of an $S_2\pi^*_\parallel$ orbital with an Rh(p_x, d_{xz}) hybrid orbital that has more p_x than d_{xz} character, while in the other there is σ overlap between an $S_2(\pi_\parallel, p_\sigma)$ hybrid and a Rh(d_{z^2}, $d_{x^2-y^2}$, p_z) hybrid orbital. Figure 14 shows contour maps of these two orbitals for comparison with the corresponding orbitals of the P_4 complex in Figure 13. Note that in the calculation for the S_2 complex the

(58) The 2P1 contribution to orbital $12a_1$ is a result of the participation of fragment orbital $4a_1$ in the interaction leading to $12a_1$. This is not shown in Figure 8.

(59) Ginsberg, A. P.; Osborne, J. H.; Sprinkle, C. R. *Inorg. Chem.* **1983**, *22*, 254.

Table XII. Electronic Absorptions and Assignments for $[RhCl(P_4)(PPh_3)_2]$

obsd values[a]				calcd energy,[b]	predicted	
λ_{max}, nm	energy, eV	ϵ, M^{-1} cm^{-1}	C_{2v} transition	eV	intensity	orbital description[c]
~365 (sh)	3.40		$7b_1 \rightarrow 12a_1$ ($^3B_1$)	3.63	w	
			$11a_1 \rightarrow 6b_2$ ($^3B_2$)	3.68	w	
339	3.66	8.0×10^3	$11a_1 \rightarrow 6b_2$ ($^1B_2$)	3.92	s	Rh $d_{x^2-y^2}$, $d_{z^2} \rightarrow$ 2P2 pσ^*
			$7b_1 \rightarrow 12a_1$ ($^1B_1$)	3.97	s	P1 p_x, s $\rightarrow$ Rh d_{z^2}, $d_{x^2-y^2}$; Rh $d_{xz} \rightarrow$ P1 p_x, s
289	4.29	3.8×10^4	$7b_1 \rightarrow 4a_2$ ($^1B_2$)	4.13	m	Rh $d_{xz} \rightarrow$ 2P2 $\pi_\perp^*$
			$5b_2 \rightarrow 6b_2$ ($^1A_1$)	4.15	s	Rh $d_{yz} \rightarrow$ 2P2 pσ^*
			$7b_1 \rightarrow 8b_1$ ($^1A_1$)	4.24	m	Rh $d_{xz} \rightarrow$ 2P2 $\pi_\perp$
			$11a_1 \rightarrow 12a_1$ ($^1A_1$)	4.27	s	Rh $d_{x^2-y^2}$, $d_{z^2} \rightarrow$ P1 p_xs
~278 (sh)	4.46		$11a_1 \rightarrow 7b_2$ ($^1B_2$)	4.49	m	Rh $d_{x^2-y^2}$, $d_{z^2} \rightarrow$ 2P2 $\pi^*_\parallel$, sσ^*
			$11a_1 \rightarrow 8b_1$ ($^1B_1$)	4.50	m	Rh $d_{x^2-y^2}$, $d_{z^2} \rightarrow$ 2P2 $\pi_\perp$
			$6b_1 \rightarrow 12a_1$ ($^1B_1$)	4.52	s	Rh $d_{xz} \rightarrow$ P1 p_x, s
			$5b_2 \rightarrow 4a_2$ ($^1B_1$)	4.53	w	Rh $d_{yz} \rightarrow$ 2P2 $\pi^*_\perp$
			$5b_2 \rightarrow 12a_1$ ($^1B_2$)	4.56	w	Rh $d_{yz} \rightarrow$ Rh d_{z^2}, $d_{x^2-y^2}$
~269 (sh)	4.61		$3a_2 \rightarrow 6b_2$ ($^1A_1$)	4.58	w	Rh $d_{xy} \rightarrow$ Rh d_{yz}, 2P2 pσ^*
			$5b_2 \rightarrow 7b_2$ ($^1A_1$)	4.64	m	Rh $d_{yz} \rightarrow$ 2P2 $\pi^*_\parallel$, sσ^*

[a] Spectra of samples dissolved in EPA glass at liquid-nitrogen temperature; measured from 800 to 260 nm. Extinction coefficients are corrected for solvent contraction on cooling to liquid-nitrogen temperature. The spectrum of $[RhBr(P_4)(PPh_3)_2]$ is almost identical with that of the chloride: λ_{max} (ϵ_{max}) = ~375 (sh), 340 (8.0×10^3), 295 (2.4×10^4), ~277 (sh), ~268 (sh). [b] Spin-unrestricted transition-state calculations. [c] The most important components contributing to the transition intensity.

molecule was oriented with the S_2 group in the *xz* plane while in the present work the bonding edge of the P_4 molecule lies in the *yz* plane. The maps show that the in-plane π overlap, which makes the most important contribution to both the Rh–P_4 and Rh–S_2 bonds, is somewhat weaker in the Rh–S_2 case. Also, the Rh–S_2 $\pi_\parallel$ orbital has its charge mainly in the S_2 spheres while in the Rh–P_4 case the charge in the $\pi_\parallel$ orbital is more nearly equally distributed between the Rh and 2P2 spheres. The weak σ interaction is quite different in Rh–P_4 and Rh–S_2 because of the different orbital hybridization on 2P2 and S_2. In both cases the σ-bonding orbital is also bonding for the coplanar ligands. In the case of the P_4 complex, the competition between the Cl and P_4 for σ bonding with the Rh results in a weakened Rh–Cl σ interaction compared to what is found for the fragment molecule (see Figures 13c and 15). This is consistent with the observed trans lengthening of the Rh–Cl bond, which is ca. 0.035 Å longer than in $[Rh(PPh_3)_3Cl]$.

SCF-Xα calculations have shown that both π and σ M–S_2 overlaps are greater in $[Ir(S_2)(PH_3)_4]^+$ than in the rhodium complex.[59] This is partly a result of relativistic expansion of the d orbitals leading to improved metal–ligand overlap. A similar effect is expected in the Ir(η^2-P_4) system and should lead to strengthening of the M–P_4 bond.

In terms of the D–C–D model,[55] η^2-Rh–P_4 bonding is expected to consist of 2P2 p$\pi_\parallel$ $\rightarrow$ Rh d_σ σ bonding together with Rh d_π $\rightarrow$ 2P2 p$\pi^*_\parallel$ π back-bonding. This description is in fairly good agreement with the results of the Xα analysis. The D–C–D σ bond corresponds to the interaction in level $8a_1$ and differs from the Xα result in neglecting the contribution of the 2P2 pσ electrons. The D–C–D π back-bond corresponds to the interaction in level $2b_2$, and the Xα description also calls for Rh d_π–2P2 p$\pi^*_\parallel$ overlap.

Valence Electron Distribution on Rh and P_4. Table X indicates that η^2-coordination of a P_4 molecule to a C_{2v} $[RhCl(PH_3)_2]$ fragment is accompanied by transfer of 0.38 e from the P_4 molecule to the fragment. The transferred charge ends up mostly on the Cl atom (0.23 e) with a smaller amount on the PH_3 groups (0.15 e); the charge on the metal atom is unchanged. There is no significant difference in the net charges of the metal-bound (2P2) and unbound (2P3) P_4 phosphorus atoms. There is, however, a great difference in how the charge is distributed over the basis functions for these two sets of atoms. As shown by Table XI, the most important difference is that 2P2 has increased pσ^* and decreased pσ occupancy compared to 2P3. Increased pσ^* occurpancy results from the $\pi_\parallel$ Rh–2P2 interaction in which metal d_{yz} charge is donated to the b_2 component of the empty P_4 $1t_1$ orbital (cf. level $5b_2$ of the complex). Decreased pσ occupancy

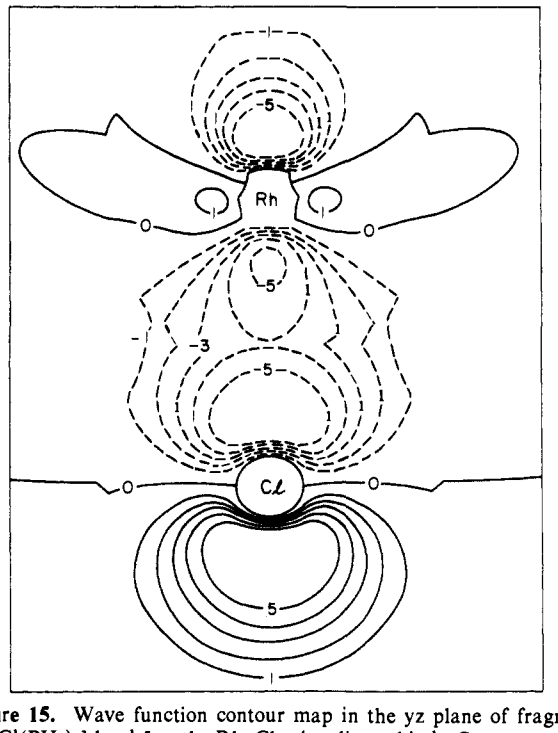

Figure 15. Wave function contour map in the yz plane of fragment $[RhCl(PH_3)_2]$ level $5a_1$, the Rh–Cl σ-bonding orbital. Contour magnitudes and sign convention are as in Figure 13.

comes about because of the σ Rh–2P2 interaction in which charge from the a_1 component of the P_4 1e orbital is donated to the empty d_{z^2}, $d_{x^2-y^2}$ metal hybrid orbital. Increased pσ^* and decreased pσ occupancy for 2P2 vs. 2P3 is consistent with the observed lengthening (by ca. 0.25 Å) of the P2–P2 compared to the P3–P3 edge. Table XI predicts a bond order of 0.4 for P2–P2 and of 1.0 for P3–P3.

Electronic Spectrum. Figure 16 shows the electronic absorption spectrum of $[RhCl(P_4)(PPh_3)_2]$ in the 250–800-nm region. $[RhBr(P_4)(PPh_3)_2]$ has an almost identical spectrum. Table XII gives the band assignments and the calculated energies for the transitions as obtained by spin-unrestricted transition-state calculations on $[RhCl(P_4)(PH_3)_2]$. The assignments were made by associating with each absorption the one-electron transitions which are in best agreement with it in regard to energy and intensity. Transition intensities were estimated qualitatively (predicted in-

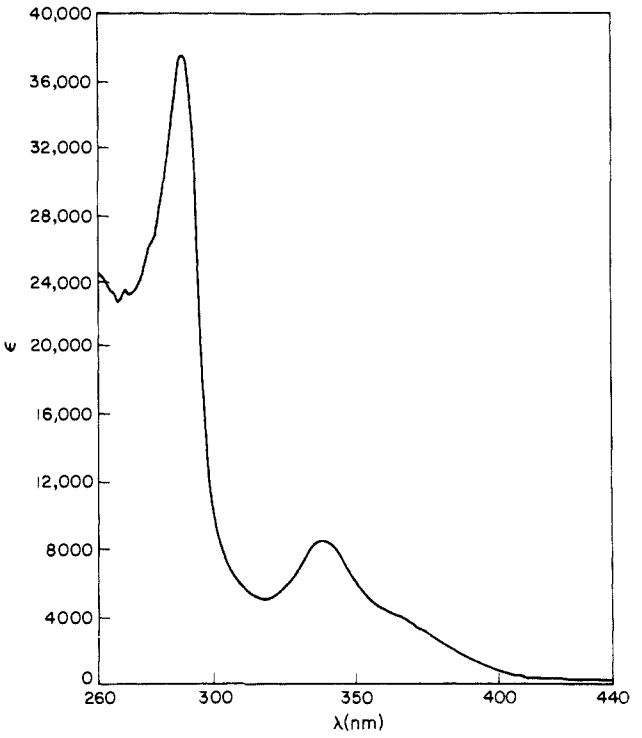

Figure 16. Electronic absorption spectrum of $[RhCl(P_4)(PPh_3)_2]$ in EPA glass at liquid nitrogen temperature.

tensity in Table XII), as described previously.[60]

As may be seen from Table XII, the agreement between observed and calculated spectra is reasonably good. With the exception of the weak shoulder at ~365 nm, the lowest energy feature in the spectrum, all of the absorptions are assigned as dipole- and spin-allowed transitions from one of the five highest energy occupied levels to one of the five lowest energy virtual levels. All dipole-allowed, spin-allowed transitions in the range of interest are accounted for in Table XII. The weak ~365-nm feature is much lower in energy than any of these transitions; it is assigned to the two lowest energy spin-forbidden dipole-allowed transitions.[61] All other spin-forbidden transitions occur close to spin-allowed transitions and do not give rise to distinct bands, although they presumably make small contributions to the observed bands. The bands in the spectrum of the η^2-P_4 complex owe most of their intensity to metal → P_4 and metal → phosphine charge transfer. Some phosphine → metal charge-transfer character is present in the 339-nm band, and Rh d–d transitions contribute to the ~278- and ~269-nm features.

Chemical Behavior and Electronic Structure. Since the Xα calculation has provided a description of the valence MO's of $[RhCl(\eta^2\text{-}P_4)(PH_3)_2]$, we can now rationalize certain aspects of its behavior and point out some possibilities which have not yet been realized. Addition of electrons to the Rh–2P2 $\pi^*_{\parallel}$ LUMO is expected to weaken or cancel the π component of the Rh–P_4 bond. We therefore expect that coordination of an electron donor ligand, reduction, or photochemical excitation of the η^2-P_4 complex will all lead to dissociation of P_4. Reduction and photochemical excitation have not yet been investigated, but coordination of $[RhCl(P_4)(PPh_3)_2]$ with CO or tertiary phosphines is found to lead to loss of P_4. Interestingly though, reaction of CO with $[RhCl(P_4)(AsPh_3)_2]$ leads to loss of $AsPh_3$ instead of P_4, presumably because in the arsine complex an Rh–As antibonding orbital is lower in energy than the Rh–P_4 antibonding orbital. The HOMO of the η^2-P_4 complex is weakly Rh–PH_3 bonding and P3–P3 $\pi^*_{\parallel}$ in character. Removal of one or two electrons from the HOMO will have little effect on the geometry or bond strength in the complex. We therefore predict that careful oxidation of $[RhCl(\eta^2\text{-}P_4)(PPh_3)_2]$ will lead to cationic η^2-P_4 complexes.

We have seen that η^2-coordination of a P_4 molecule to $[RhCl(PPh_3)_2]$ causes only a very slight change in the tetrahedral edge opposite to the bound edge. This suggests that bridging di(η^2)-P_4 complexes might be possible, although it is clear from Figure 9 that access to the back edge of the P_4 ligand is sterically hindered. From an orbital point of view, coordination of $RhCl(PR_3)_2$ to orbital $8b_1$ of $[RhCl(\eta^2\text{-}P_4)(PH_3)_2]$ would give the bridging complex. However, addition of $RhCl(PR_3)_2$ to $[RhCl(\eta^2\text{-}P_4)(PH_3)_2]$ would most likely lead to dissociation of P_4 because of coordination to the LUMO. Indeed this is what occurred when $[RhCl(PPh_3)_3]$ was mixed with $[RhCl(P_4)(PPh_3)_2]$.

Comparison of Xα and Extended Hückel Calculations. EHMO theory is an approximate semiempirical method notable for its ease of use and ability to give qualitative insights into the nature of molecular bonding. The SCF–Xα–SW method, on the other hand, is a quantitative first-principles procedure able to provide detailed information about the electronic structure and spectra of transition-metal complexes. Since we have applied both of these methods to $[RhCl(\eta^2\text{-}P_4)(PH_3)_2]$, it is of interest to note the extent to which the EHMO results approximate the Xα results. In making this comparison it must be remembered that in the EHMO model complex P_4 was tetrahedral with a P–P distance of 2.21 Å while the Xα model used the X-ray parameters of $[RhCl(\eta^2\text{-}P_4)(PPh_3)_2]$, in which the bonded edge of the P_4 molecule is expanded to 2.46 Å.

Both the EHMO and SCF–Xα calculations have led to the conclusion that the η^2-Rh–P_4 bond is well described by the D–C–D model and that the coordinated P–P bond is weakened by its interaction with the metal. Beyond this general qualitative agreement the EHMO results diverge significantly from the Xα picture. First of all, the EHMO description of the P_4 molecule reverses the order of the 1e and $2t_2$ levels from that found in the Xα and all other MO calculations.[5-9] A similar discrepancy occurs in the P_4 complex, where the EHMO calculation reverses the order of orbitals $11a_1$ and $7b_1$ as well as $6b_2$ and $4a_2$, to give both the HOMO and LUMO different from the Xα results. In the case of the LUMO, the disagreement would be corrected by an EHMO calculation in which the bonded P_4 edge is expanded to 2.46 Å; this should lower the energy of the b_2 orbital enough to make it the LUMO.[52] A major variance between the EHMO and Xα results occurs in the description of the charge distribution in $[RhCl(\eta^2\text{-}P_4)(PH_3)_2]$: According to the EHMO calculation the coordinated P_4 carries a net charge of −1.34, while the Xα results indicate a net charge of +0.38. This disagreement would probably increase if the EHMO calculation were carried out with the coordinated P_4 edge expanded to the observed length.

Acknowledgment. W.E.L. thanks the SERC (UK) and the Royal Society (London) for support. We thank Professor T. A. Albright for sending us a preprint of his work (ref 52).

Supplementary Material Available: Thermal parameters (Table II), structure factors, hydrogen atom coordinates, and crystal packing diagram (34 pages). Ordering information is given on any current masthead page.

(60) Ginsberg, A. P.; O'Halloran, T. V.; Fanwick, P. E.; Hollis, L. S.; Lippard, S. J. *J. Am. Chem. Soc.* **1984**, *106*, 5430.

(61) The dipole-forbidden singlet HOMO–LUMO transition is predicted at 3.68 eV and probably also contributes to the ~365 nm shoulder. The dipole- and spin-forbidden HOMO–LUMO triplet transition is predicted at 3.48 eV but is expected to be too weak to be observed under the conditions of our experiment.

(62) The periodic group notation in parentheses is in accord with recent actions by IUPAC and ACS nomenclature committees. A and b notation is eliminated because of wide confusion. Groups IA and IIA become groups 1 and 2. The d-transition elements comprise groups 3 through 12, and the p-block elements comprise groups 13 through 18. (Note that the former Roman number designation is preserved in the last digit of the new numbering: e.g., III → 3 and 13.)